Coupled body and surface wave sensitivity kernels for coda-wave interferometry in a three-dimensional scalar scattering medium

Andres Barajas, Ludovic Margerin, Michel Campillo

Geophysical Journal International

Geophys. J. Int. (2022) **230,** 1013–1029
Advance Access publication 2022 April 9
GJI Seismology

https://doi.org/10.1093/gji/ggac091

Coupled body and surface wave sensitivity kernels for coda-wave interferometry in a three-dimensional scalar scattering medium

Andres Barajas [1], Ludovic Margerin[2] and Michel Campillo[1]

[1] *Institut des Sciences de la Terre, Observatoire des Sciences de l'Univers de Grenoble, Université Grenoble Alpes, Grenoble,* 38610*, France, E-mail: custore@gmail.com*

[2] *Institut de Recherche en Astrophysique et Planétologie, Observatoire Midi-Pyrénées, Université Paul Sabatier, Toulouse,* 31400*, France*

Accepted 2022 March 7. Received 2022 February 28; in original form 2021 June 10

SUMMARY

Analysis of long recordings of ambient seismic noise has shown to be effective for estimation of seismic responses between points located on the surface. This includes both the ballistic and the coda part of the waveforms. Passive image interferometry is used to analyse perturbations in the reconstructed coda, to detect and locate changes in the medium. This method has been shown to be effective in monitoring variations in seismic velocity produced by a wide range of phenomena. However, localization of the sources of these changes is still an open problem for a 3-D half-space, given the difficulties of integrating body and surface waves within the same framework. In this study, we approach this problem by developing the sensitivity kernels of a scalar model that integrates the body and surface scalar waves. First, we establish a parallel between the penetration depth of the surface waves for the elastic and scalar cases, which equips the latter with a natural scaling with frequency that is otherwise not included in the model. Next, using a variational approach, we quantify how a velocity perturbation in the medium affects the propagation velocity of the surface waves. Based on these results, we extend the sensitivity theory to include the body and surface waves as modes of propagation and detection, as restricted to a 1-D depth-dependent perturbation description, for simplicity. The obtained kernel can be expressed as the sum of a surface and a body waves sensitivity kernels, which are inter-dependent through a set of traveltime distributions. These distributions are estimated with Monte Carlo simulations based on the radiative transfer equations of the system, with the source and the receiver located in the same position at the surface. The sensitivity at depth is in good agreement with previous results based on full wavefield elastic simulations in 3-D inhomogeneous half-space. The temporal evolution of the body and surface waves sensitivity is quantified, as well as the contribution of all the possible modes of propagation and detection to each of these sensitivities. We show how the position of the source affects the sensitivity between the two types of waves. We find that the efficacy of energy conversion from surface to body waves is controlled by the ratio between the surface wave penetration depth and the mean free path, a feature that has not been reported in previous studies. This means that configurations that share this ratio have the same sensitivity as long as all the spatial and temporal variables (e.g. elapsed time, depth) are non-dimensionalized with the mean free path and the mean free time, respectively.

Key words: Coda waves; Seismic interferometry; Wave scattering and diffraction.

1 INTRODUCTION

The heterogeneities in the Earth crust interact with passing seismic waves and scatter them in multiple directions. This phenomenon is directly related to the formation of the coda, which contains information about the strength and properties of this interaction. The first study in this direction was by Aki (1969), where he defined for the first time the coda and its principal characteristics. The coda was later used to analyse the attenuation properties related to the structure of the Earth (Aki & Chouet 1975). More studies followed that showed that variations in the amplitude and phase of scattered waves allowed identification of small perturbations in the properties of the crust (Poupinet *et al.* 1984; Ratdomopurbo & Poupinet 1995; Schaff & Beroza 2004). Estimation of these changes from

the continuous seismic noise field is one of the fundamental principles of passive image interferometry, which has been shown to be effective for detection of velocity variations of fault zones (Wegler & Sens-Schönfelder 2007; Brenguier *et al.* 2008) and volcanoes (Sens-Schönfelder & Wegler 2006), or as a consequence of various meteorological phenomena (Meier *et al.* 2010; Hillers *et al.* 2014; Wang *et al.* 2017). Zeng (2006) and Sato (1994) have shown the importance of each mode of wave propagation and their possible conversions, in the formation of the seismic coda, suggesting that the scattered wave energy at different arrival times may be dominated by different types of waves. Maeda *et al.* (2008) made important contributions in this regard, modelling the coda envelopes in an inhomogeneous elastic half-space including *P*, *SV* and Rayleigh waves in the single scattering approximation.

The phase changes generated in the coda depend on the location of the perturbation and the time that the seismic field has to sample it. This means that it is possible to locate the perturbation in the crust with the information registered at the surface at different times. Coda wave interferometry establishes the link between these two through introduction of the sensitivity kernels. The first kernels were deduced for the diffusive regime (Pacheco & Snieder 2005), and then for the single scattering regime (Pacheco & Snieder 2006) of the scalar case. The traveltime sensitivity kernel is a density function that shows the most probable sectors through which a wave passes when going from the source to the receiver at a given lapse time. The kernel can be calculated as a convolution of the probabilities of the particle traveling from either the source or the receiver, to each part of the medium that is sampled by the waves (Pacheco & Snieder 2005). Each of these probabilities can be interpreted physically as the intensity received at one point in the space after a unitary pulse is emitted from another (Margerin *et al.* 2016). Later, Margerin *et al.* (2016) demonstrated the importance of the directionality of the seismic field, which implied that an analysis of the sensitivity based only on the energy intensities was insufficient. To solve this, they developed sensitivity kernels through specific intensities, overcoming the restrictions on the propagation regime that was previously limited to the diffusive or the single-scattering cases, and extending the theory towards anisotropic scattering events.

The sensitivity kernels have been tested in full wavefield simulations (Kanu & Snieder 2015; Planes *et al.* 2015) and applied to real field data to detect changes in the medium preceding a volcanic eruption (Obermann *et al.* 2013a; Lesage *et al.* 2014) or associated with earthquakes (Obermann *et al.* 2014). The coupling between body and surface waves has remained a challenging factor in the development of the sensitivity kernels in a 3-D half-space, which is the usual setting for most seismic applications. Obermann *et al.* (2013b, 2016) developed a heuristic approach to this problem by expressing the sensitivity as a linear combination of two independent sensitivities, one for surface waves and the other for body waves, with a controlling factor mediating the two that changes with time, and that is estimated through full wavefield numerical simulations. This factor helps to recreate predominance of surface and body wave sensitivities at different lapse times. This method has been extended to localize small-scale perturbations in media (Obermann *et al.* 2019).

Recently, Margerin *et al.* (2019) developed a scalar model based on the Helmholtz equation in a half-space with Robin boundary conditions (Hein 2010), that naturally integrates body and surface waves, allowing them to estimate the mean free paths and times of the two modes and establish the radiative transfer equations. Based on this model, we reformulate the sensitivity equations from a probabilistic point of view to include the two types of propagation and to estimate the times the waves pass in each mode through a series of Monte Carlo simulations. This allows us to obtain the traveltime density distributions between the two modes of propagation for different depths in a 3-D half-space medium. In parallel, we estimate the phase perturbations of the surface waves as a consequence of a perturbation in the medium, and integrate this with the results of the simulations, to obtain the sensitivity kernel. We finally compare the performance of this kernel with previous studies, and analyse its most important features.

2 SCALAR MODEL

We begin with a quick overview of the scalar model developed by Margerin *et al.* (2019). First, we state the wave equation in a 3-D half-space

$$(\rho\partial_{tt} - T\Delta)\, u(t, \mathbf{r}, z) = 0, \tag{1}$$

where, t is time, $(\mathbf{r}, z)$ is the position vector $(\mathbf{r}, z \geq 0)$, ρ is the density, T is the elastic constant of the medium and u is the displacement. The existence of surface waves is ensured, thanks to the Robin boundary condition over the surface,

$$(\partial_z + \alpha)u(t, \mathbf{r}, z)|_{z=0} = 0, \tag{2}$$

where α is a positive constant. For time harmonic fields ($u \propto \mathrm{e}^{-i\omega t}$), eq. (1) reduces to the Helmholtz equation:

$$\Delta u(\mathbf{r}, z) + k^2 u(\mathbf{r}, z) = 0, \tag{3}$$

where k is the wavenumber ($k = \omega/c$). The first kind of solution of these equations is the sum of the incident and reflected body waves:

$$u_b(t, \mathbf{r}, z) = A(\mathrm{e}^{-iqz} + r(q)\mathrm{e}^{iqz})\mathrm{e}^{i(\mathbf{k}_\parallel \cdot \mathbf{r} - \omega t)}, q \geq 0, \tag{4}$$

where $\mathbf{k}_\parallel = (k_x, k_y, 0)$ is the horizontal wavenumber, with $\mathbf{k}_\parallel \cdot \mathbf{k}_\parallel + q^2 = \dfrac{\omega^2}{c^2}$ and

$$r(q) = \frac{q + i\alpha}{q - i\alpha}. \tag{5}$$

The second possible kind of solution is a wave propagating parallel to the surface

$$u_s(t, \mathbf{r}, z) = Ah(z)e^{i(\mathbf{k}_\parallel \cdot \mathbf{r} - \omega t)}; \tag{6}$$

where the term $h(z) = e^{-\alpha z}$, and therefore α, controls the surface wave penetration depth. In this case, the horizontal wavenumber is related to the constant α by the relation $\mathbf{k}_\parallel \cdot \mathbf{k}_\parallel - \alpha^2 = \dfrac{\omega^2}{c^2}$. Making use of the relation between the phase velocity c_R and the magnitude of the horizontal wavenumber $k_\parallel = \omega/c_R$, the former can be written as

$$c_R = \frac{c}{\sqrt{1 + \dfrac{c^2\alpha^2}{\omega^2}}}, \tag{7}$$

where c is the body wave velocity. One particularity of this system is that the surface group velocity v_g is always higher than both the body and surface wave phase velocities:

$$v_g = \frac{c^2}{c_R} = c\sqrt{1 + \frac{c^2\alpha^2}{\omega^2}}. \tag{8}$$

This implies that the first ballistic energy received at a point on the surface will come mainly from the surface waves for a source located in the vicinity of the surface. Furthermore, even in a half-space geometry, the surface wave is dispersive. To make our model

more realistic, we will show in Section 3 and Appendix A, that by letting α appropriately depend on frequency, dispersion can be eliminated so that $c = v_g$, just like for Rayleigh waves.

The field produced by a single scattering event is obtained through the perturbed Helmholtz equation

$$\Delta u(\mathbf{r}, z) + k^2(1 + \epsilon a^3 \delta(\mathbf{r})\delta(z - z_s))u(\mathbf{r}, z) = 0, \tag{9}$$

where ϵ is the local perturbation of the inverse square velocity, and a represents the typical dimension of the scatterer located at (0, 0, z_s). We assume that an incoming incident body wave or surface wave, $u_0(\mathbf{r}, z)$, is scattered by a weak scatterer, under the condition that the wavelength λ is larger than the scatterer dimension. This condition is usually expressed in terms of the wavenumber as $ka \ll 1$. Making use of the Born approximation, the produced scattered field can be written as

$$u(\mathbf{r}, z) = u_0(\mathbf{r}, z) - k^2 \epsilon a^3 G\left(\mathbf{r}, z, z_s\right) u_0\left(\mathbf{0}, z_s\right), \tag{10}$$

where $G\left(\mathbf{r}, z, z_s\right)$ represents the Green's function of the Helmholtz equation in a half-space with mixed boundary condition, which is composed of both body waves and surface waves. With this approximation, it is possible to calculate the scattering cross-section of a scatterer as a balance of the incoming and outgoing energies. From the scattering cross-sections, we can obtain the mean free times of all the possible wave conversions

This treatment is adequate, provided the free surface induces a random phase shift between the upgoing and downgoing waves, eliminating any possible interference effect (Margerin *et al.* 2019)

$$\begin{aligned}
\tau^{s\to s} &= \frac{1}{\alpha}\frac{4}{nck^3a^6\epsilon^2},\\
\tau^{s\to b} &= \frac{4\pi}{nck^4a^6\epsilon^2},\\
\tau^{b\to b} &= \frac{4\pi}{nck^4a^6\epsilon^2},\\
\tau^{b\to s}(z) &= \frac{e^{2\alpha z}}{\alpha}\frac{2}{nck^3a^6\epsilon^2},
\end{aligned} \tag{11}$$

where n is the volume density of the scatterers. The total mean free times can be calculated as

$$\begin{aligned}
\frac{1}{\tau^s} &= \frac{1}{\tau^{s\to s}} + \frac{1}{\tau^{s\to b}},\\
\frac{1}{\tau^b(z)} &= \frac{1}{\tau^{b\to s}(z)} + \frac{1}{\tau^{b\to b}}.
\end{aligned} \tag{12}$$

The dependence of $\tau^{b\to s}$ on the depth is directly related to the probability of exciting a surface wave, which is proportional to the surface eigenfunction. The ratio between the energy of surface waves and the depth-integrated energy of the body waves generated by a point source is

$$R(z) = \frac{\tau^{s\to b}}{\tau^{b\to s}(z)} = \frac{2\pi c\alpha}{\omega}e^{-2\alpha z}. \tag{13}$$

The transport of the energy of body waves can be described in terms of the specific volumetric energy density $e_b(t, \mathbf{r}, z, \hat{\mathbf{k}})$, where $\hat{\mathbf{k}}$ is a vector on the unit sphere in three dimensions. The dependence on frequency has been omitted here and in the rest of this section for simplicity. The integration of this specific volumetric energy density over a solid angle gives us the volumetric energy density

$$E_b(t, \mathbf{r}, z) = \int_{4\pi} e_b(t, \mathbf{r}, z, \hat{\mathbf{k}})\mathrm{d}\hat{k}. \tag{14}$$

On the other hand, the transport of surface waves can be described in terms of the specific surface energy density $\epsilon_s(t, \mathbf{r}, \hat{\mathbf{n}})$, where $\hat{\mathbf{n}}$ is a unit vector in the horizontal plane. To describe the system through the formulation of transport equations, it is necessary to have energy densities of equal dimensions; for this reason, the specific volumetric energy density of surface waves is introduced:

$$e_s(t, \mathbf{r}, z, \hat{\mathbf{n}}) = 2\alpha\epsilon_s(t, \mathbf{r}, \hat{\mathbf{n}})e^{-2\alpha z}, \tag{15}$$

which when integrated over depth give us back the specific surface density $\epsilon_s(t, \mathbf{r}, \hat{\mathbf{n}})$. Using this new specific volumetric density it is now possible to define a volumetric energy density of the surface waves:

$$E_s(t, \mathbf{r}, z) = \int_{2\pi} e_s(t, \mathbf{r}, z, \hat{\mathbf{n}})\mathrm{d}\hat{n}. \tag{16}$$

The total energy density at a point in the medium will be the sum of the energy densities of the body and surface waves $E_b(t, \mathbf{r}, z) + E_s(t, \mathbf{r}, z)$, which is supported by the orthogonality of their eigenfunctions.

From these definitions the radiative transport equations can be constructed. The scattered intensity for the body waves is isotropic thanks to the assumed random phase shift between the upgoing and downgoing waves body waves, while the surface part is isotropic in the horizontal plane (Margerin *et al.* 2019). The increase and decay of the intensity are stated in terms of the conversion between all the possible modes

$$\begin{aligned}
\left(\partial_t + v_g\hat{\mathbf{n}}\cdot\nabla\right)e_s(t, \mathbf{r}, z, \hat{\mathbf{n}}) &= -\frac{e_s(t, \mathbf{r}, z, \hat{\mathbf{n}})}{\tau^s} + \frac{E_s(t, \mathbf{r}, z)}{2\pi\tau^{s\to s}}\\
&\quad + \frac{E_b(t, \mathbf{r}, z)}{2\pi\tau^{b\to s}(z)} + s_s(t, \mathbf{r}, z, \hat{\mathbf{n}})\\
\left(\partial_t + c\hat{\mathbf{k}}\cdot\nabla\right)e_b(t, \mathbf{r}, z, \hat{\mathbf{k}}) &= -\frac{e_b(t, \mathbf{r}, z, \hat{\mathbf{k}})}{\tau^b(z)} + \frac{E_b(t, \mathbf{r}, z)}{4\pi\tau^{b\to b}}\\
&\quad + \frac{E_s(t, \mathbf{r}, z)}{4\pi\tau^{s\to b}} + s_b(t, \mathbf{r}, z, \hat{\mathbf{k}})
\end{aligned} \tag{17}$$

where the gradients are defined in three dimensions, and the terms $s_{s,\,b}$ are sources of the surface and body waves, generated by a unit point source at depth z_0

$$\begin{aligned}
s_s(t, \mathbf{r}, z, \hat{\mathbf{n}}) &= \frac{2\alpha R\left(z_0\right)e^{-2\alpha z}\delta(\mathbf{r})}{2\pi\left(1 + R\left(z_0\right)\right)},\\
s_b(t, \mathbf{r}, z, \hat{\mathbf{k}}) &= \frac{\delta\left(z - z_0\right)\delta(\mathbf{r})}{4\pi\left(1 + R\left(z_0\right)\right)}.
\end{aligned} \tag{18}$$

These equations ensure that the unit radiated energy from the source is distributed between surface and body waves according to the energy partitioning ratio $R(z_0)$ defined in eq. (13).

3 PENETRATION DEPTH OF THE SURFACE WAVE

One of the fundamental characterizing parameters of the interaction between body and surface waves is the penetration depth of the surface waves. For this reason, finding an equivalence between the penetration depth for the scalar model and for the elastic model is fundamental. For the elastic case, we take as reference the Rayleigh waves formed in a homogeneous half-space. The sensitivity of both surface waves to physical variations at depth is a function of their respective surface eigenfunctions, or more precisely, to the square

of these functions, which are related to their energy. The displacement eigenfunctions for the Rayleigh waves can be written as (Ben-Menahem & Singh 1981, p.115)

$$\begin{aligned} u_x(\omega;x,z) &= Ar_1(\omega;z)\sin(\omega t - k_R x),\\ r_1(\omega;z) &= \left[e^{-\gamma_\alpha k_R z} - \left(1-\frac{c_R^2}{2c_\beta^2}\right)e^{-\gamma_\beta k_R z}\right],\\ u_z(\omega;x,z) &= Ar_2(\omega;z)\cos(\omega t - k_R x),\\ r_2(\omega;z) &= \left(1-\frac{c_R^2}{c_\alpha^2}\right)^{1/2}\left[-e^{-\gamma_\alpha k_R z} + \left(1-\frac{c_R^2}{2c_\beta^2}\right)^{-1} e^{-\gamma_\beta k_R z}\right], \end{aligned} \tag{19}$$

where u_x is the displacement in the direction parallel to wave propagation, u_z is the displacement perpendicular to the surface, A represents the amplitude of the wave, c_α and c_β are the velocities of the P and S waves, respectively, k_R is the wavenumber of the Rayleigh waves and the gamma factors are

$$\gamma_\alpha = \left(1-\frac{c_R^2}{c_\alpha^2}\right)^{1/2} \qquad \gamma_\beta = \left(1-\frac{c_R^2}{c_\beta^2}\right)^{1/2}. \tag{20}$$

The energy density of the Rayleigh wave averaged over one cycle can be written in terms of r_1 and r_2 as (Aki & Richards 2002, p.287)

$$\frac{1}{2}\rho\left(r_1^2(\omega;z) + r_2^2(\omega;z)\right), \tag{21}$$

where ρ is the density of the medium. We want to find a function in the form of a simple exponential that resembles the shape and, especially, the reach of the Rayleigh energy density function, so we can compare it directly with the function that describes the scalar surface eigenfunction. In eq. (19), the penetration at depth of the energy is dominated by the exponential function with the lower exponent, which in the case of a Poisson solid is $e^{-\gamma_\beta k_R z}$, where $\gamma_\beta = 0.39$. We take a slightly modified version of this function that better resembles the elastic wave at shallow depths, without significantly changing its reach, $e^{-0.3k_R z}$; this is the equivalent scalar surface eigenfunction. A comparison between these can be seen in Fig. 1. Although their shape is not exactly equal (which would be technically impossible with the simplifications made), they both have relatively similar reaches and shapes.

As the scalar surface eigenfunction is also $h(z) = e^{-\alpha z}$, it is clear that the parameter α must be equal to $\alpha = 0.3k_R$. It is important to note that the behaviour here that is illustrated in Fig. 1 is completely independent of the Rayleigh wavelength λ_R, and that this equivalence between the elastic and scalar cases provides with natural scaling with the frequency for the latter. This implies that α is now frequency dependent, thus removing the original dispersive nature of the scalar surface waves, as can be seen from eq. (7). Furthermore, this fixes the group velocity to the surface wave velocity $U = C_R$, as is demonstrated in Appendix A.

We take $L_s = 2\alpha^{-1}$ as the penetration depth of the scalar surface wave, as at this depth the amplitude of the eigenfunction is ∼14 per cent of its amplitude at the surface. To compare this penetration with the elastic case, we can write L_s in terms of the Rayleigh wavelength, using the proposed equivalence between these two cases

$$L_s = 2\alpha^{-1} = 2(0.3k_R)^{-1} \approx 1.06\lambda_R. \tag{22}$$

This result is consistent with the rule of thumb that estimates the penetration of Rayleigh waves at around 1 horizontal wavelength λ_R.

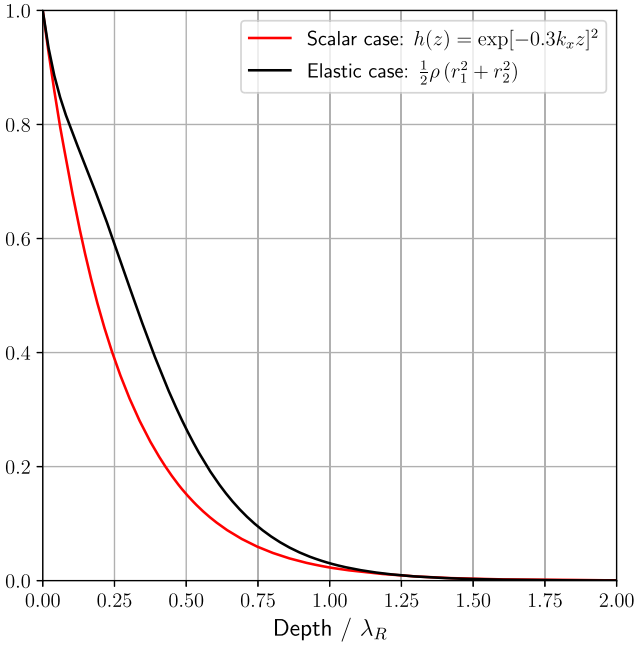

Figure 1. Comparison of the penetration depths of the energy of the Rayleigh waves and a simplified model. Both have normalized amplitudes.

4 SURFACE WAVE PHASE VELOCITY SENSITIVITY

In this section, we describe the effects of a bulk velocity perturbation on the phase velocity of the scalar surface wave. The interactions of a surface wave with a perturbation in the medium is one of the principal mechanisms that control the responses that are recorded at the surface. This interaction is different from that of the body waves, in the sense that the surface waves propagate as a whole over a volume close to the surface, which implies that any small change in one layer of the medium within its penetration depth should affect the whole wave. In particular, we are interested in determining how the surface phase velocity changes with a fractional change in the bulk velocity. To do so, we follow variational principles applied to the Langrangian of surface waves (Aki & Richards 2002, p.283). The Lagrangian of this system is

$$L = \frac{1}{2}\left[\rho(\partial_t u_s(t,\mathbf{r},z))^2 - T(\nabla u_s(t,\mathbf{r},z))^2 + \alpha T u_s(t,\mathbf{r},z)^2\delta(z)\right], \tag{23}$$

where $u_s(t,\mathbf{r},z)$ is the surface wave solution defined in eq. (6), and terms at the right-hand side of this equation represent the kinetic energy, the potential energy and an elastic potential energy at the surface associated with the boundary condition, respectively. The last term is necessary to implement the boundary condition in eq. (2), while leaving unchanged the wave propagation in eq. (1) (Margerin *et al.* 2019). This negative elastic potential is what allows the system to sustain the propagation of surface waves. A boundary term in the Lagrangian can be found in the treatment of a fluid–solid boundary in elastodynamics (Dahlen & Tromp 2021, p.70), or in the case of a vibrating string with one end elastically attached (Gelfand & Fomin 1963, p.155). We integrate the Lagrangian over depth, and average it over one cycle, to put it in the form of the energy integrals:

$$\int_0^\infty \langle L\rangle \mathrm{d}z = \frac{1}{2}\left[\omega^2 I_1 - k_\parallel^2 I_2 - I_3 + I_s\right], \tag{24}$$

where

$$I_1 = \frac{1}{2}\int_0^\infty \rho h^2 \mathrm{d}z, \qquad I_2 = \frac{1}{2}\int_0^\infty T h^2 \mathrm{d}z,$$
$$I_3 = \frac{1}{2}\int_0^\infty T\left(\frac{\mathrm{d}h}{\mathrm{d}z}\right)^2 \mathrm{d}z, \qquad I_s = \frac{1}{2}\int_0^\infty \alpha T h^2 \delta(z)\mathrm{d}z. \tag{25}$$

The integrated Lagrangian is stationary for a perturbation of the surface eigenfunction, as demonstrated in Appendix B:

$$\omega^2 \delta I_1 - k_\parallel^2 \delta I_2 - \delta I_3 + \delta I_s = 0, \tag{26}$$

where δI represents the perturbation or variation of the functional I (Gelfand & Fomin 2000, p.8). On the other hand, Appendix C shows that the integrated Lagrangian in eq. (24) is equal to zero for the surface eigenfunction, as is expected from energy conservation. This leads to the following relationship:

$$\omega^2 I_1 = k_\parallel^2 I_2 + I_3 - I_s. \tag{27}$$

We proceed to find the change in the surface wave phase velocity as a consequence of a perturbation in the medium. To do so, we include a perturbation in the eigenfunction at fixed frequency $h + \delta h = h(\rho + \delta\rho, T + \delta T, k_\parallel + \delta k_\parallel, \omega)$, in the Lagrangian

$$\begin{aligned}
&\omega^2 \int_0^\infty (\rho + \delta\rho)(h + \delta h)^2 \,\mathrm{d}z \\
&= (k_\parallel + \delta k_\parallel)^2 \int_0^\infty (T + \delta T)(h + \delta h)^2 \,\mathrm{d}z \\
&+ \int_0^\infty (T + \delta T)\left[\frac{\mathrm{d}}{\mathrm{d}z}(h + \delta h)\right]^2 \mathrm{d}z \\
&- \int_0^\infty \alpha (T + \delta T)(h + \delta h)^2 \,\delta(z)\mathrm{d}z.
\end{aligned} \tag{28}$$

Eliminating perturbations of the second order, and subtracting the previously known relationships between the energy integrals, we obtain

$$\begin{aligned}
\int_0^\infty -2k_\parallel \delta k_\parallel T h^2 \,\mathrm{d}z = &\int_0^\infty k_\parallel^2 \delta T h^2 \,\mathrm{d}z + \int_0^\infty \delta T \left(\frac{\mathrm{d}h}{\mathrm{d}z}\right)^2 \mathrm{d}z \\
&- \int_0^\infty \omega^2 \delta\rho h^2 \,\mathrm{d}z - \int_0^\infty \alpha \delta T h^2 \delta(z)\,\mathrm{d}z.
\end{aligned} \tag{29}$$

From this we can calculate the change in phase velocity

$$\left(\frac{\delta c_R}{c_R}\right)_\omega = -\frac{\delta k_\parallel}{k_\parallel} = \frac{\int_0^\infty \left[k_\parallel^2 h^2 + \left(\frac{\mathrm{d}h}{\mathrm{d}z}\right)^2\right]\delta T \mathrm{d}z - \int_0^\infty \omega^2 h^2 \delta\rho \mathrm{d}z - \int_0^\infty \alpha \delta T h^2 \delta(z)\mathrm{d}z}{2k_\parallel^2 \int_0^\infty T h^2 \mathrm{d}z}. \tag{30}$$

To simplify this expression, we assume that there is no perturbation of the density ($\delta\rho = 0$), and that the background elastic constant T does not depend on the depth. We also assume that the elastic constant is not perturbed at the surface ($\delta T(z = 0) = 0$), as a way to avoid perturbations over the boundary conditions or over the surface elastic energy that supports the surface waves. The result is formally similar to the expression that describes the phase velocity changes for Love waves in the elastic case (Aki & Richards 2002, p.285)

$$\left(\frac{\delta c_R}{c_R}\right)_\omega = \frac{\rho c^2}{2k_\parallel^2 I_2}\int_0^\infty \left[k_\parallel^2 h^2 + \left(\frac{\mathrm{d}h}{\mathrm{d}z}\right)^2\right]\frac{\delta c}{c}(z)\mathrm{d}z, \tag{31}$$

where I_2 is the energy integral defined in eq. (25), and where we made use of the relationships between the rigidity and the bulk velocity $\delta T/T = 2\delta c/c, T = \rho c^2$. The kernel of this integral can be written as

$$K_{C_{\mathrm{ph}}}(z) = \frac{\rho c^2}{2k_\parallel^2 I_2}\left[k_\parallel^2 h^2 + \left(\frac{\mathrm{d}h}{\mathrm{d}z}\right)^2\right]. \tag{32}$$

This equation shows that any possible variation in the bulk velocity will change the surface wave velocity as long as it happens within the penetration depth determined by the surface eigenfunction h.

5 TIME DENSITIES

Having established how a bulk perturbation affects the surface wave velocity, we move into another fundamental aspect of the response at the surface: in what proportion is this response related to the body waves or the surface waves. For this, we study the typical time a packet of energy or seismic phonon (Shearer & Earle 2004) passes through each part of the medium, and the typical time it spends in each mode of propagation (here, as a body or surface wave). In our theoretical approach, each body wave phonon may assume any direction in 3-D space, and the reflection B.C. at the surface is treated at the level of the energy conservation equation, meaning that the upgoing phonon and its downgoing reflection are a single particle. This treatment is adequate, provided the free surface induces a random phase shift between the upgoing and downgoing waves, eliminating any possible interference effect (Margerin *et al.* 2019). We analyse the phonon propagation taking a probabilistic approach similar to the one presented by Zhang *et al.* (2021) for 2-D elastic waves. We begin by using A to denote the emission of the seismic phonon at time $t_0 = 0$ from the source, B to denote the event of a phonon propagating in time t' through the medium, and C to denote the phonon arriving at the receiver. The time will be implicitly included in the differentiation between the events A, B, and C. The probability of each event will be written as $P(E)$ where E represents the event. The state of each phonon in one event is specified with a subindex that indicates its position $\mathbf{r}$, its direction $\mathbf{k}$, or its mode of propagation m; the mode is b or s when the phonon propagates as a body or surface particle, respectively. For example, $P(B_{z',b'})$ is the probability that the phonon is detected at time t' as a body particle at depth z', independent of its radial position $\mathbf{r}$ or the direction of propagation $\mathbf{k}$. Therefore, $P(B_{b'})$ is the probability that the phonon was propagating at time t' as a body particle, irrespective of its position or its direction. Naturally, $P(B_{b'})$ is the sum of $P(B_{z',b'})$ for all the depths, which for a continuous system can be written as

$$P(B_{b'}) = \int_{z'} P(B_{z',b'})\mathrm{d}z'. \tag{33}$$

In general, removing an index of an event probability implies grouping all the events designated by that index by summing their individual probabilities

$$P(E_{i,j}) = \sum_k P(E_{i,j,k}). \tag{34}$$

We can divide the event into subsets with any classification index we want as long as it covers the original set completely; in other words, under the condition that it forms a sample space of the original event (Miller & Childers 2012, p. 8).

The probability that a phonon arrives at the receiver at $\mathbf{r}$ under the condition that it was emitted at the source in $\mathbf{r_0}$, can be written as the conditional probability $P(C_{\mathbf{r}} \mid A_{\mathbf{r_0}})$ (Gut 2013, p. 16). We can rewrite this in terms of the conditional probabilities with an

intermediate state of propagation, using the Chapman–Kolmogorov equation (Ross 2014, p. 195; Papoulis & Pillai 2002, p. 254; Roepstorff 2012, p. 5)

$$P(C_{\mathbf{r}} \mid A_{\mathbf{r_0}}) = \int_{\omega} P(C_{\mathbf{r}} \mid B_{\omega}) P(B_{\omega} \mid A_{\mathbf{r_0}})\, \mathrm{d}\omega, \tag{35}$$

where ω represents every possible intermediate state. Eq. (35) indicates that the probability of going from event A to C can be found from the probabilities of the phonon going from A to B and from B to C, as long as we add all the possible intermediate events B. The sample space can be classified in different ways: e.g., we can specify the event B uniquely for its position, and this would effectively cover the whole range of possibilities.

$$P(C_{\mathbf{r}} \mid A_{\mathbf{r_0}}) = \int_{\mathbf{r}'} P(C_{\mathbf{r}} \mid B_{\mathbf{r}'}) P(B_{\mathbf{r}'} \mid A_{\mathbf{r_0}})\, \mathrm{d}\mathbf{r}'. \tag{36}$$

However, this selection would only allow us to describe a set or particles in which the propagation direction of each of the phonons is independent of its position, which is the case for a diffusive regime, as was proposed by Pacheco & Snieder (2005). Therefore, the classification set is closely related to the underlying physical model that describes the propagation regime. If we want to describe the first stages of a particle propagation, this description is inadequate, as the propagation directions are marked by the strong directionality of the phonons (Margerin *et al.* 2016). Therefore, we classify all the possible states of one particle travelling from the source to the receiver through a combination of its position, direction, and mode of propagation

$$P(C_{\mathbf{r}} \mid A_{\mathbf{r_0}}) = \int_{\mathbf{r}'} \int_{\mathbf{k}'} \sum_{m} P(C_{\mathbf{r}} \mid B_{\mathbf{r}',\mathbf{k}',m}) P(B_{\mathbf{r}',\mathbf{k}',m} \mid A_{\mathbf{r_0}})\, \mathrm{d}\mathbf{k}'\, \mathrm{d}\mathbf{r}', \tag{37}$$

where $\mathbf{k}'$ was not specified in the source or the arrival events because at this point every possible direction of propagation of the phonons is considered. Note that integration of eq. (37) over all directions (and modes) does no lead to eq. (36), because this implies a joint integration between the two conditional probabilities sharing the same $\mathbf{k}'$. Integrating eq. (37) over the time of the propagation event B (t') for all the possible traveltimes (between 0 and t), and reorganizing the terms, gives

$$t = \int_{\mathbf{r}'} \left[\int_0^t \int_{\mathbf{k}'} \sum_{m} \frac{P(C_{\mathbf{r}} \mid B_{\mathbf{r}',\mathbf{k}',m}) P(B_{\mathbf{r}',\mathbf{k}',m} \mid A_{\mathbf{r_0}})}{P(C_{\mathbf{r}} \mid A_{\mathbf{r_0}})}\, \mathrm{d}\mathbf{k}' dt' \right] \mathrm{d}\mathbf{r}' \tag{38}$$

The square parentheses in eq. (38) were added to highlight that the term inside them is what has been previously called the traveltime sensitivity kernel (Margerin *et al.* 2016), which was extended to track the two possible modes of propagation and the directionality of the seismic particles. It must be noted, however, that this is not the half-space traveltime sensitivity kernel, as it does not have the phase velocity sensitivity of the surface waves integrated yet. To differentiate more clearly between the two, we define the time density as

$$\bar{t}_m(\mathbf{r_0}, \mathbf{r}', \mathbf{k}', \mathbf{r}) = \int_0^t \frac{P(C_{\mathbf{r}} \mid B_{\mathbf{r}',\mathbf{k}',m}) P(B_{\mathbf{r}',\mathbf{k}',m} \mid A_{\mathbf{r_0}})}{P(C_{\mathbf{r}} \mid A_{\mathbf{r_0}})} dt' \tag{39}$$

It is clear that when the time density is integrated over all space, in every possible direction and summed over all modes, it is equal to the traveltime as shown in eq. (38). A less general expression for the time sensitivity can be obtained integrating over the propagation directions or over certain spatial directions, which will allow us to conveniently simplify or cluster together different stages of the propagation of the phonons. To simplify eq. (38) and to approach the measurements made by an observer of many random walks that begin at a single point, we assume that we are only interested in the phonons emitted by the source at location $\mathbf{r}' = 0$ (i.e. the source in the surface). This allows the references to event A to be dropped:

$$t = \int_0^t \int_{\mathbf{r}'} \int_{\mathbf{k}'} \sum_{m} \frac{P(C_{\mathbf{r}} \mid B_{\mathbf{r}',\mathbf{k}',m}) P(B_{\mathbf{r}',\mathbf{k}',m})}{P(C_{\mathbf{r}})}\, \mathrm{d}\mathbf{k}' \mathrm{d}\mathbf{r}' \mathrm{d}t'. \tag{40}$$

Using the Bayes formula (Papoulis & Pillai 2002, p32; Gut 2013, p. 17)

$$P(C_{\mathbf{r}} \mid B_{\mathbf{r}',\mathbf{k}',m}) P(B_{\mathbf{r}',\mathbf{k}',m}) = P(B_{\mathbf{r}',\mathbf{k}',m} \mid C_{\mathbf{r}}) P(C_{\mathbf{r}}), \tag{41}$$

we can rewrite eq. (40) as

$$t = \int_0^t \int_{\mathbf{r}'} \int_{\mathbf{k}'} \sum_{m} P(B_{\mathbf{r}',\mathbf{k}',m} \mid C_{\mathbf{r}})\, \mathrm{d}\mathbf{k}' \mathrm{d}\mathbf{r}' \mathrm{d}t'. \tag{42}$$

Through this simplification, we can now integrate over all directions

$$t = \int_0^t \int_{\mathbf{r}'} \sum_{m} P(B_{\mathbf{r}',m} \mid C_{\mathbf{r}})\, \mathrm{d}\mathbf{r}' \mathrm{d}t'. \tag{43}$$

Now, we proceed to make the contribution of each mode explicit, and to simplify the spatial dependence, with integration over the whole space for the surface mode, and over the horizontal plane for the body mode. This leads to the following expression:

$$t = \int_0^t P(B_{s'} \mid C_{\mathbf{r}})\, \mathrm{d}t' + \int_0^t \int_{z'} P(B_{z',b'} \mid C_{\mathbf{r}})\, \mathrm{d}z' \mathrm{d}t'. \tag{44}$$

The surface mode propagates always parallel to the surface and its exact depth is immaterial; for this reason, its probability was fully integrated. Before going any further, it is useful to interpret each of these probabilities as a counting process. Let us imagine that we shoot a great number of seismic phonons from the source, some of which reach the receiver at time t; if we receive a high enough number of particles, their travel histories will be representative of all the possible paths from the source to the receiver. This is the set of particles that fulfil the condition in each of the conditional probabilities of eq. (44), and that arrive at the receiver located at $\mathbf{r}$ in time t. As these represent the whole set of possibilities, the estimation of one probability can be done by counting; for example if we want $P(B_{z',b'} \mid C_{\mathbf{r}})$, we just have to count the number of body wave particles that were at position z' in time t', and divide this number by the total of the particles that arrived at the receiver. Therefore, eq. (44) can be written as

$$t = \int_0^t \frac{N_s(t')}{N}\, \mathrm{d}t' + \int_0^t \int_{z'} \frac{N_b(z', t')}{N}\, \mathrm{d}z' \mathrm{d}t'. \tag{45}$$

This indicates an interesting relationship: the integration of the probability that a particle propagates in a certain mode between all the possible traveltimes is equivalent to the sum of the time spent by all the particles in that mode, divided by the total number of particles; or in other words, this is equivalent to the average time spent in that mode $\bar{t}_m$:

$$\bar{t}_m = \int_0^t \frac{N_m(t')}{N}\, \mathrm{d}t' = \int_0^t P(B_{m'} \mid C_{\mathbf{r}})\, \mathrm{d}t'. \tag{46}$$

Using this terminology, eq. (44) can be written as

$$t = \bar{t}_s + \int_{z'} \bar{t}_b(z')\, \mathrm{d}z' \tag{47}$$

by restating a known property of the elapsed times. Note that we use the same notation as in eq. (39) because $\bar{t}_s$ and $\bar{t}_b(z')$ are actually time densities associated to the surface and body phonons respectively, but integrated over all directions, over the horizontal plane for the body particles, and over the whole space for the surface particles. Before applying this new notation, let us come back to the probability description in eq. (44). Up to this point, the mode on which the seismic phonon arrives to the receiver has been ignored. However, this can be made explicit by addition of the probabilities at the arrival point

$$\begin{aligned} t = &\frac{P(C_{\mathbf{r},s})}{P(C_{\mathbf{r}})}\int_0^t P(B_{s'} \mid C_{\mathbf{r},s})\,\mathrm{d}t' \\ &+\frac{P(C_{\mathbf{r},b})}{P(C_{\mathbf{r}})}\int_0^t P(B_{s'} \mid C_{\mathbf{r},b})\,\mathrm{d}t' \\ &+\frac{P(C_{\mathbf{r},s})}{P(C_{\mathbf{r}})}\int_0^t\int_{z'} P(B_{z',b'} \mid C_{\mathbf{r},s})\,\mathrm{d}z'\mathrm{d}t' \\ &+\frac{P(C_{\mathbf{r},b})}{P(C_{\mathbf{r}})}\int_0^t\int_{z'} P(B_{z',b'} \mid C_{\mathbf{r},b})\,\mathrm{d}z'\mathrm{d}t' \end{aligned} \tag{48}$$

as $P(C_{\mathbf{r},\mathbf{m}})$ the probability of the phonon arriving at time t and in mode m, at the receiver located at (r, z). Before, the surface mode was not subclassified at different depths, because it propagates as a whole in a direction parallel to the surface. However, at the arrival point, it becomes necessary as the energy of the surface waves is highly dependent on the depth, and therefore the position of the receiver will determine how strongly it is detected. The quantities in the form $P(C_{\mathbf{r},\mathbf{m}})/P(C_{\mathbf{r}})$ can be interpreted as the fraction of particles that arrive in a given mode m with respect to the total of the particles that arrive at the receiver. Given that each of these phonons represents a packet of energy that follows the propagation scheme described by the transfer eqs. (17), this fraction can be written as $E^m(t, \mathbf{r})/E(t, \mathbf{r})$, where $E^m(t, \mathbf{r})$ is the energy that arrives in mode m at the receiver, and $E(t, \mathbf{r})$ the total energy that arrives at the same point. Using this equivalence and integrating for all the possible traveltimes t' results in

$$\begin{aligned} t = &\frac{E^s(t,r,z)}{E(t,r,z)}\bar{t}_{s\to s}(t,r,z) + \frac{E^b(t,r,z)}{E(t,r,z)}\bar{t}_{s\to b}(t,r,z) \\ &+\frac{E^s(t,r,z)}{E(t,r,z)}\int_0^\infty \bar{t}_{b\to s}(z';t,r,z)\,\mathrm{d}z' \\ &+\frac{E^b(t,r,z)}{E(t,r,z)}\int_0^\infty \bar{t}_{b\to b}(z';t,r,z)\,\mathrm{d}z'. \end{aligned} \tag{49}$$

The semicolon in the arguments of each average time separates the variables of the propagation from the variables of the detection, and the subindex indicates the temporal sequence of propagation and detection. For example, $\bar{t}_{s\to b}$ is the average time that the particles that arrived in body wave mode passed into surface wave mode. These times are schematized in Fig. 2 for two simplified cases. Also, the position of the receiver $\mathbf{r}$ was explicitly put in terms of the depth and the radial distance, which exploits the cylindrical symmetry of the half-space. Eq. (49) shows the time of flight distribution of the particles according to their mode of propagation, and the depth (for the body waves) at which they propagate. Note how the terms denominated by t are dimensionally different: for the propagation of body particles, we have times per unit of depth ($t_{b\to s}$ and $t_{b\to b}$), and for the surface waves, they are simply times ($t_{s\to s}$ and $t_{s\to b}$). Eq. (49) describes what parts of the medium and what modes of the propagation are preferred for particles traveling from the source to the receiver: a spatial and modal 'distribution' of the total traveltime. We define the effective time spent in each mode

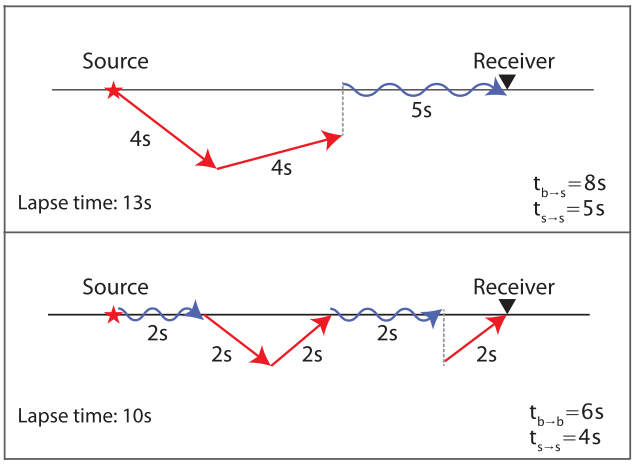

Figure 2. Representation of the propagation times and modes for two simple cases. Top: an arrival in surface wave mode. Bottom: an arrival in body wave mode.

as an energy-weighted average between the two possible modes of arrival

$$\begin{aligned} \langle t_s(t,r,z)\rangle = &\frac{E^s(t,r,z)}{E(t,r,z)}\bar{t}_{s\to s}(t,r,z) \\ &+\frac{E^b(t,r,z)}{E(t,r,z)}\bar{t}_{s\to b}(t,r,z) \\ \langle t_b(z';t,r,z)\rangle = &\frac{E^s(t,r,z)}{E(t,r,z)}\bar{t}_{b\to s}(z';t,r,z) \\ &+\frac{E^b(t,r,z)}{E(t,r,z)}\bar{t}_{b\to b}(z';t,r,z) \end{aligned} \tag{50}$$

These equations show us the contributions of each of the modes of propagation independent of the mode of arrival at the receiver. The effective times can be replaced in eq. (49) to obtain

$$t = \langle t_s(t,r,z)\rangle + \int_0^\infty \langle t_b(z';t,r,z)\rangle\,\mathrm{d}z', \tag{51}$$

reconstructing once again an intuitive result through the implicit contributions of the possible transitions of the particles. Finally, it is worth noting that eq. (49) can be re-arranged differently, as

$$\begin{aligned} t = &\frac{E^s(t,r,z)}{E(t,r,z)}\left(\bar{t}_{s\to s}(t,r,z) + \int_0^\infty \bar{t}_{b\to s}(z';t,r,z)\,\mathrm{d}z'\right) \\ &+\frac{E^b(t,r,z)}{E(t,r,z)}\left(\bar{t}_{s\to b}(t,r,z) + \int_0^\infty \bar{t}_{b\to b}(z';t,r,z)\,\mathrm{d}z'\right) \end{aligned} \tag{52}$$

in which each sum inside the parentheses is equal to the arrival time t. From eq. (52), it is easier to analyse some particular cases: e.g., if the receiver is located at great depth, then the surface waves will not reach it (which implies that $E^s = 0$ and $E^b = E$) and eq. (52) will turn into

$$t = \bar{t}_{s\to b}(t,r,z) + \int_0^\infty \bar{t}_{b\to b}(z';t,r,z)\,\mathrm{d}z' \tag{53}$$

which is a simplified version of eq. (51) with the effective times replaced by the averaged times.

6 SENSITIVITY KERNELS

We proceed now to integrate the time densities and the surface phase velocities into the sensitivity kernels. Let us assume that, on average, the particles that propagate as body waves pass an effective time

$\langle t_b(z^{'})\rangle$ in a layer at depth $z^{'}$, which has a slight velocity perturbation δc. The overall traveltime change is then $\delta t = -\langle t_b(z^{'})\rangle(\delta c/c)$. For the time spent as surface waves, the traveltime perturbation will have an analogous expression using the relative surface wave velocity perturbation $\delta t = -\langle t_s\rangle(\delta c_R/c_R)$. Therefore, the effective traveltime delay generated by any set of perturbations in the medium can be written as

$$\delta t = -\langle t_s(t,r,z)\rangle\frac{\delta c_R}{c_R} - \int_0^\infty \langle t_b(z';t,r,z)\rangle\frac{\delta c}{c}(z')\mathrm{d}z'. \tag{54}$$

Putting the relative surface phase velocity perturbation in terms of δc at a layer at depth $z^{'}$ with eq. (31) allows calculation of the apparent velocity variation ($\delta t/t = -\varepsilon$) in terms of the bulk velocity variation

$$\frac{\delta t}{t}(t,r,z) = \int\left(-\frac{\langle t_s(t,r,z)\rangle}{t}K_{C_{\mathrm{ph}}}(z') - \frac{\langle t_b(z';t,r,z)\rangle}{t}\right)\frac{\delta c}{c}(z')\mathrm{d}z'. \tag{55}$$

The term between parentheses is the sensitivity kernel K; the left part is the surface wave sensitivity K_s and the right part is the body wave sensitivity K_b. The negative signs indicate that an increase in the velocity in the medium ($\delta c/c > 0$) generates an early phase arrival ($\delta t/t < 0$). Replacing the effective times by their definitions (eq. 50) gives

$$\begin{aligned}\frac{\delta t}{t}(t,r,z) = -\int\Bigg(&\frac{E^s(t,r,z)}{E(t,r,z)}K_{s\to s}(z';t,r,z)\\ &+\frac{E^b(t,r,z)}{E(t,r,z)}K_{s\to b}(z';t,r,z)\\ &+\frac{E^s(t,r,z)}{E(t,r,z)}K_{b\to s}(z';t,r,z)\\ &+\frac{E^b(t,r,z)}{E(t,r,z)}K_{b\to b}(z';t,r,z)\Bigg)\frac{\delta c}{c}(z')\,\mathrm{d}z',\end{aligned} \tag{56}$$

where

$$\begin{aligned}K_{s\to s}(z';t,r,z) &= \frac{\bar{t}_{s\to s}(t,r,z)}{t}K_{C_{\mathrm{ph}}}(z')\\ K_{s\to b}(z';t,r,z) &= \frac{\bar{t}_{s\to b}(t,r,z)}{t}K_{C_{\mathrm{ph}}}(z')\\ K_{b\to s}(z';t,r,z) &= \frac{\bar{t}_{b\to s}(z';t,r,z)}{t}\\ K_{b\to b}(z';t,r,z) &= \frac{\bar{t}_{b\to b}(z';t,r,z)}{t}.\end{aligned} \tag{57}$$

These equations show the contribution of each mode to the sensitivity and depth dependence on the energy density of surface and body waves.

7 MONTE CARLO SIMULATIONS

Monte Carlo simulations to recreate properties of the propagation of seismic waves were originally done in equivalent acoustic systems. These simulations successfully reproduced features like coda envelopes generated by earthquakes, and the attenuation in different scattering regimes (Gusev & Abubakirov 1987; Abubakirov & Gusev 1990; Hoshiba 1991). This was later extended to models that includes depth dependence of the velocity structure and the mean free path (Hoshiba 1997; Margerin *et al.* 1998), elastic propagation modes (Margerin *et al.* 2000; Przybilla *et al.* 2006), lateral heterogeneous scattering and nonisotropic scattering (Sens-Schönfelder *et al.* 2009; Sanborn *et al.* 2017), and coupling between surface and body scalar waves (Margerin *et al.* 2019). Here, the last case will be further explored towards estimation of the traveltime sensitivity kernels of both body and surface waves.

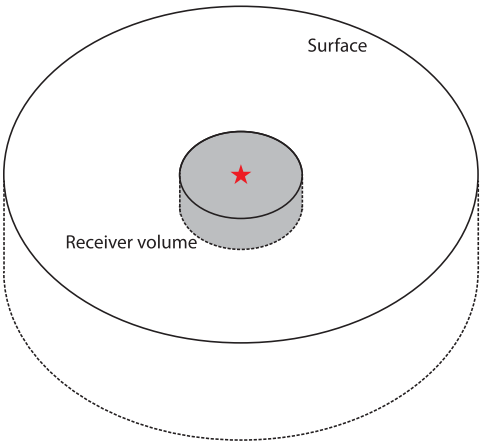

Figure 3. Model of the Monte Carlo simulations. Red star, location of the source; grey volume, receiver zone.

7.1 General outline

The Monte Carlo simulations are aimed to provide measurements of the time spent by a phonon at each depth and mode in a half-space medium, when traveling from the source to the receiver. The general procedure consists of shooting many seismic particles from the source, and allowing them to travel in a straight line until they are scattered; after each of these scattering events, a new direction and propagation mode are chosen randomly following a certain probability distribution. The time between scattering events is statistically controlled by the mean free time of each mode. The receiver is defined as a small, finite volume through which the particles must pass to contribute to the energy density and to the sensitivity measured from that point, at that particular time. This is the particle counting method (Gusev & Abubakirov 1987; Sens-Schönfelder *et al.* 2009). One of the main disadvantages of this method is that the probability that a particle that is doing a random walk will pass through the receiver at a given time is low; this is partially compensated for by shooting many particles from the source, and by exploiting the symmetries of the medium, which can allow the receiver to be turned into a bigger volume. For example, in a full-space medium, the receiver can be a spherical volume. The half-space symmetry allows one to consider ring-shaped receivers around the source. In our case, the source and the receiver are in the same position, and therefore this last has a cylindrical shape, as illustrated in Fig. 3. It is worth noting that the symmetry can be broken if the sources are non-isotropic, although this is not the case here.

Potentially the main advantage of the particle counting method is that it allows the trajectories of all the phonons to be followed, and the time that each of them passes in every part of the medium and for every mode to be measured. With these measurements, we can calculate the time densities for each mode and depth, which are the basis of the sensitivity kernel, as was explained in the previous sections. Next, we present the most important aspects of the simulations.

(i)*Propagation.* Many particles (10^9 in this case) are shot in random directions from a source located at the surface, with the initial modes chosen probabilistically to follow eqs. (18). The body mode propagates in three dimensions, and the surface mode in two. This means that the surface particles do not have any depth coordinates. Each particle propagates in a straight line in a random isotropic direction, as assigned at the beginning. The time of propagation or the free time of flight, is also chosen randomly, in such a way that its distribution reconstructs the exponential probability density function $\tau^{-1}e^{t/\tau}$ (Welch *et al.* 2011, chapter 5, p. 6), where τ is the mean free time. This mean free time is chosen according to the mode and depth of the particle (for the body particles), as indicated in eq. (12). For the body waves, the dependence of the mean free time on the depth is simplified through the method of delta collisions, which introduce virtual scattering events that do not modify the direction of propagation (Lux & Koblinger 2018, p. 222). If a body particle reaches the surface, its movement is completely reflected into the half-space without modifying any other parameter.

(ii)*Scattering.* Once the simulation time reaches the free time of flight, a scattering event occurs. A new propagation direction and mode are chosen. The mode is chosen randomly between the two possible outcomes, using their respective mean free times as weights for each option. For example, the probability that a body wave scatters into a surface wave is

$$p^{b\to s}(z) = \frac{(\tau^{b\to s}(z))^{-1}}{(\tau^{b\to s}(z))^{-1} + (\tau^{b\to b})^{-1}}. \tag{58}$$

It follows then that the probability that a body wave scatters into another body wave is $p^{b\to b} = 1 - p^{b\to s}$. Note that for this particular case, when the body particle is far away from the surface, the probability of changing into a surface particle is practically zero. When a surface particle scatters into a body particle, the depth of the particle is defined randomly following the probability density function $2\alpha e^{-2\alpha z}$, which represents the normalized energy density of the surface waves.

(iii)*Time bookkeeping.* To measure the time densities in eq. (49), the half-space is virtually segmented into horizontal layers. When the particle is propagating as a body wave, we keep track of the time spent in each of these layers. These times, t_b, are added together when the particle passes through the same layer several times. If the particle propagates as a surface wave, the time is registered and accumulated as the independent value t_s. This process is illustrated in Fig. 4. It is important to remember that although from the book-keeping process the times recorded in the body or surface modes appear to be equivalent, for the body waves the measure is technically the time per unit of layer length, contrary to the case of the surface waves, where the total time is measured directly, as was explained in Section 5.

(iv)*Detection and averaging.* The source and the receiver are both located at the same position in the surface, to reproduce the measurements of the seismic field obtained through the autocorrelation of ambient noise measurements. However, in practice, the receiver is a cylindrical volume (Fig. 3): the particle has arrived at the receiver only if it is inside this volume at a given lapse time. If this is the case, the book-kept times are registered along with the mode of the particle at that instant (i.e. the arrival mode). The simulation continues independently of the arrival of the particle, as it is possible that the particle will be within the receiver volume for another measurement at a later lapse time.

After all the particle paths have been simulated, the registered times are averaged together for particles that arrived in the same mode at the receiver at a given time, t, and that propagated at the same mode and at the same depth (for body waves). This procedure gives us all the averaged times in eq. (49).

8 COUPLED SURFACE AND BODY WAVE SENSITIVITY

8.1 Sensitivity profile at depth

We performed a series of Monte Carlo simulations to analyse the responses on the surface produced by a velocity perturbation of a layer at depth, and the participation of each of the modes of propagation to this response. The parameters used in the simulations are given in Table 1. We estimate the apparent velocity variation ($-\delta t/t$) for a velocity perturbation of 20 per cent with a thickness of 50 m (i.e. the grid spacing of the model) located at different depths. The results are represented as the orange line in Fig. 5. This is done by taking each of the values of the discretized version of the kernel in eq. (55) and multiplying them by $\delta c/c = 0.2$. We can see that the same velocity perturbation generates strong traveltime perturbations when located close to the surface. The magnitude of these phase perturbations can decrease by one order of magnitude when the bulk velocity perturbation is displaced 1 km deeper into the medium.

Given that the sensitivity is the addition of the interdependent surface and body sensitivities, we can track what part of this velocity variation is due to the surface and body wave sensitivity independently; this is represented by the solid blue and red lines in Fig. 5. The body and surface sensitivities show some expected characteristics: the surface sensitivity becomes negligible at around 0.7 km depth, which is the imposed reach of the surface waves. On the other hand, the body sensitivities show a deeper reach that is related to the transit of the body wave particles to deeper zones of the medium, and their eventual return. This snapshot of the depth dependence of the sensitivity at short lapse-time shows dominance of the surface sensitivity in the zones closer to the surface (i.e. within the first 300 m) and a limited reach of the body wave sensitivity to the first couple of kilometres. Fig. 5 also shows the contribution of each possible combination of propagation and detection modes to the apparent velocity variation. For example, in the Figure, the dotted blue line (i.e. contribution of $K_{s\to b}$) shows the contribution of the surface wave particles that arrived in the body wave mode, and the dashed blue line (i.e. contribution of $K_{s\to s}$) shows the contribution of the surface wave particles that arrived in the surface wave mode; with the solid blue line as the weighted average between the two of these (as can be seen in eqs. 56 and 57). The sensitivity on a given mode is always higher when the arrival happens in the same mode; for example the contribution of $K_{b\to b}$ is higher than the contribution of $K_{b\to s}$. At this lapse time ($t/\tau^{b\to b} = 5.7$), there is still a low number of scattering events, and therefore a low probability of changing mode. However, the total surface and body wave sensitivities (Fig. 5, solid blue and red lines) appear to be closer to the surface mode arrivals (Fig. 5, dashed lines), which indicates that the number of surface phonons at the receiver is higher. This is related to the location of the receiver on the surface, and is a common feature for all the data obtained with this configuration.

We proceed now to measure how the sensitivity at depth changes with the lapse time. The temporal evolution of the profile for the surface and body sensitivity kernels can be seen in Fig. 6. In general, there is a decrease in surface sensitivity and an increase in body sensitivity related to the radiation of this type of wave into the bulk of the medium (Margerin *et al.* 2019). The amplitude of the surface

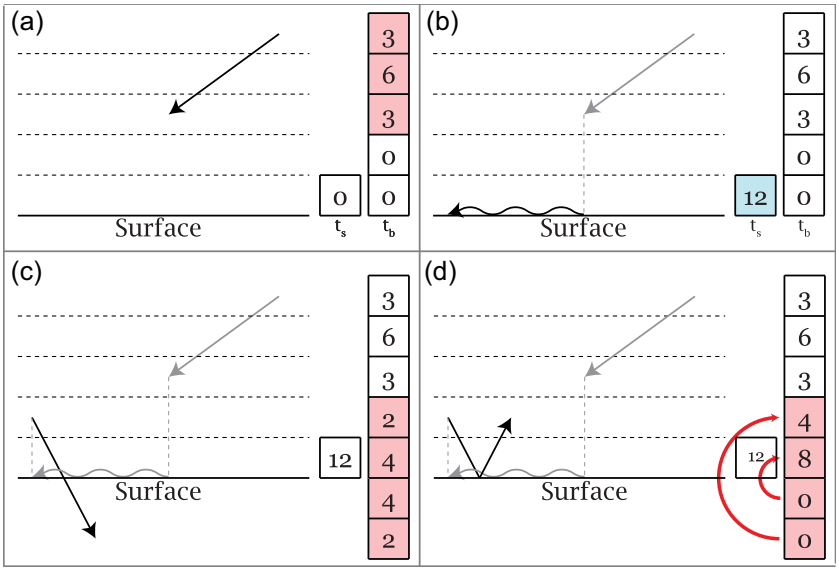

Figure 4. Time bookkeeping for body and surface waves. The probabilistic character of the time between the scattering events has been simplified. The time between the scattering events is 12 s. (a) Time spent by the body particles is recorded independently for each layer. (b) Time spent as a surface particle is recorded independently. (c) If the surface particle turns into a body particle, the probability of appearing at a certain depth is controlled by the surface energy density. When the body particle reaches the surface, the time is recorded temporarily in layers beyond it. (d) Times beyond the surface are reflected and summed with the layers within the half-space.

Table 1. Parameters used in the Monte Carlo simulations. The last two parameters are only relevant for the absorbing boundary conditions. The parameters with an asterisk might differ from Obermann *et al.* (2016), for reasons explained in the main text. The parameters with a dagger were not defined or not measured in this study.

Variable	Monte Carlo
frequency∗ (Hz)	5.25
$\alpha^{\dagger}$ (km^{-1})	2.86
Surface penetration depth L_s (km)	0.7
B. energy velocity c_E (km s^{-1})	3.9
S. energy velocity c_R (km s^{-1})	3.7
Mean free time $\tau^{b\to b}$ (s)	0.35
Mean free time $\tau^{b\to s}\vert_{z=0}{}^{\dagger}$ (s)	1.64
Mean free time $\tau^{s\to b\dagger}$ (s)	0.35
Mean free time $\tau^{s\to s\dagger}$ (s)	0.33
Mean free path $l^{b\to b}$ (km)	1.37
Mean free path $l^{b\to s}\vert_{z=0}{}^{\dagger}$ (km)	0.63
Mean free path $l^{s\to b\dagger}$ (km)	1.30
Mean free path $l^{s\to s\dagger}$ (km)	1.22
Grid spacing g_r (m)	50
Receiver radius∗ (km)	5.7
Receiver depth∗ (m)	20
Model depth (km)	6
Model radius∗ (km)	5.7
$1/(na^6\epsilon^2)$ (km^{-3})	558.2

wave sensitivity changes gradually, but its shape remains the same. This peculiarity comes from the manifest independence between $K_{C_{ph}}(z')$ and $\langle t_s(t,\, r,\, z)\rangle$, which acts as a modulating pre-factor (see eq. 55). The deeper zones of the medium are sampled only by the body waves, as their sensitivity extends over these regions at later lapse times. The surface wave sensitivity dominates in regions close to the surface, especially at early lapse times, and both types of sensitivities decrease in the vicinity of the surface at longer lapse times.

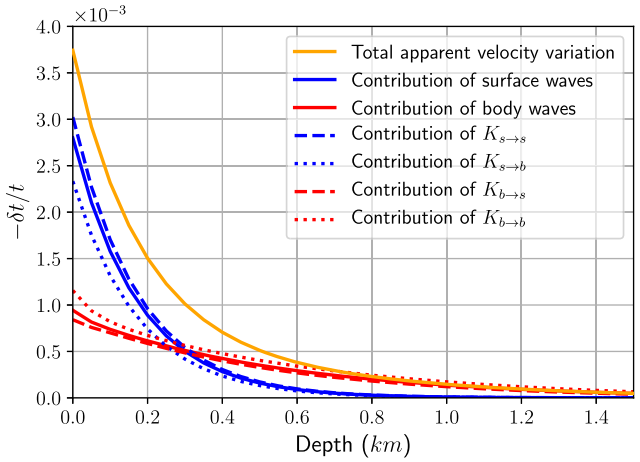

Figure 5. Total apparent velocity variation (orange) associated with the body wave sensitivity (red), the surface wave sensitivity (blue) and each of the time densities in eqs (56) and (57) at a lapse time of 2 s (normalized time of $t/\tau^{b\to b} = 5.7$) with a velocity perturbation of $\delta c/c = 0.02$.

8.2 Comparison with numerical simulations for elastic waves

A previous numerical study of the sensitivity in an elastic 3-D half-space was made by Obermann *et al.* (2016). The model they use had a square cross-section of side 10 km and total depth 6 km, with absorbing boundary condition applied at the bottom and all across the lateral area of the model. The apparent velocity perturbation was estimated by comparing the waveforms obtained without and with a horizontal velocity perturbation located at different depths in an elastic medium. They first estimate the surface and body wave contributions to the apparent velocity variation independently; the surface contribution $\varepsilon^{\mathrm{Surf}}$ is determined through a series of simulations in a 3-D homogeneous elastic half-space elastic medium. The body wave contribution, $\varepsilon^{\mathrm{Body}}$, is estimated by substituting the mean

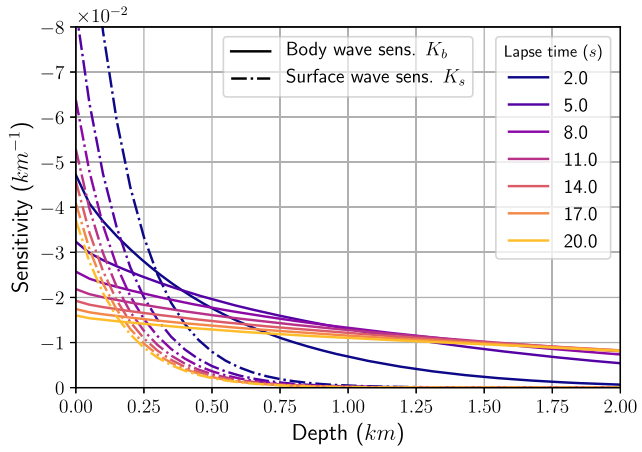

Figure 6. Profile of the surface (dashed lines) and body (solid lines) wave sensitivity kernels at depths, for the different lapse times (as indicated by the colours).

intensity predicted by radiative transfer theory in the kernel for the diffusive regime by Pacheco & Snieder (2005).

The authors further assume that the total apparent velocity variation can be modelled as a linear combination of the independent contributions of body and surface waves

$$\varepsilon^{\text{model}}(z,t) = \alpha'(t)\varepsilon^{\text{Surf}}(z) + (1-\alpha'(t))\varepsilon^{\text{Body}}(z,t) \tag{59}$$

where α' is the fitting parameter that they called the partition coefficient (the prime was added to differentiate it from the surface penetration factor of the scalar case α). Then, they performed a series of simulations in a heterogeneous medium and, at each time, searched for the partition coefficient α' that optimizes the fit between $\varepsilon^{\text{model}}$ and the measured total apparent velocity variation at depths.

The parameters used initially in the Monte Carlo simulation were chosen to resemble the physical variables of Obermann *et al.* (2016), to compare our results with those presented in their work (Table 1). Some clarifications must be made about some of these values: α was chosen to match the reach of the surface wave sensitivity reported in Obermann *et al.* (2016) of $L_s = 0.7$ km. This automatically fixes a value of the frequency to 5.25 Hz through the relationship explained in Section 3. Obermann *et al.* (2016) use a source frequency of 20 Hz to obtain the same penetration depth of the surface waves; the source of the discrepancy could be the fact that Obermann *et al.* (2016) make a broad-band simulation, meaning that the frequency content of the seismic field can change as consequence of the interaction of the waves with the complex medium, whereas in our case the simulation is quasi-monochromatic. Therefore, it is possible that a physical mechanism (as a frequency-dependent scattering, for example) could reduce the main frequency of the waves in the medium producing the penetration depth reported for the surface wave sensitivity. The absorbing boundary conditions of the simulations of Obermann *et al.* (2016) can be easily implemented in a Monte Carlo random walk by addition of the condition that the simulation ends once a particle leaves the allowed zone. The boundary conditions are only used when explicitly stated to facilitate the comparison between the two studies. In the case of Obermann *et al.* (2016), the propagation volume was rectangular (with a side length of 10 km), while here we make use of a symmetric cylindrical zone. We choose the radius in such a way that the total horizontal area would be approximately the same (100 km^2). Finally, the mean free path $l^{b\to b}$ is adjusted (in this case, to 1.37 km), through the choice of the parameters ϵ, a and n, or more specifically, through the factor $1/(na^6\epsilon^2)$ in eq. (11). This automatically fixes the values of the rest of the mean free paths and the mean free times. Any change in this factor will change the mean free paths and the mean free times in the same proportion, as this factor is common to all of them. It must be noted that within the factor $1/(na^6\epsilon^2)$ the dimension of the scatterer a, and the local perturbation of the inverse squared velocity ϵ, can be as small as necessary to fulfil the conditions under which we can apply the Born approximation ($ka\epsilon \ll 1$). It is also important to remark that these parameters comply with the conditions of validity of the transport theory as $kl^b \approx 3.7 > 1$. This value was obtained using the smallest mean free path which occurs at the surface for the body particles.

The sensitivity at depth obtained by Obermann *et al.* (2016) is shown in Fig. 7(a), where the orange line represents the observed apparent velocity variation measured in full elastic simulations, the dashed black line is the result of the model fitted with eq. (59), and the dashed red line represents the estimation only due to the body sensitivity kernel calculated by substituting the mean intensity predicted by radiative transfer theory into equation of Pacheco & Snieder (2005). To compare with our case, we also imposed absorbing boundary conditions and recalculated the apparent velocity variation; the result is shown in Fig. 7(b) (right-hand panel). The resemblance between the two studies is remarkable, especially if we keep in mind that one of them was obtained from full elastic wavefield simulations and the other from a simple scalar model.

8.3 Time partition coefficient

We also estimated the contributions of surface and body waves to the apparent velocity variations. These are proportional to their corresponding sensitivities. The total contribution of each can be represented by eq. (51) as

$$1 = \frac{\langle t_s(t,r,z)\rangle}{t} + \frac{\langle t_b(t,r,z)\rangle}{t} = \eta_s(t) + \eta_b(t) \tag{60}$$

where the average time spent as a body particle is integrated for all the depths. The terms on the right-hand side of eq. (60) are the time partition coefficients. These represent the time that a typical phonon passes in each mode (as a fraction between 0 and 1), and are therefore proportional to the relative participation of each mode of propagation to the total sensitivity. Any changes that increase the total time spent in the body wave mode (e.g. moving the receiver to a deeper layer) will necessarily produce a decrease in the total time spent in the surface wave mode. We can make an analogous definition of the partition coefficients in terms of K_s and K_b (which implies inclusion of the variations in the surface wave velocity with perturbations at depth $K_{C_{ph}}$). However, the preference here is to keep these in terms of the time densities, as their interpretation is more immediate. We can classify the participation in the sensitivity by the mode of propagation and detection simultaneously, using eq. (52)

$$1 = \frac{E^s(t,r,z)}{E(t,r,z)}(\eta_{s\to s} + \eta_{b\to s}) + \frac{E^b(t,r,z)}{E(t,r,z)}(\eta_{s\to b} + \eta_{b\to b}) \tag{61}$$

where each sum inside the parentheses is equal to 1:

$$\begin{aligned} \eta_{s\to s} + \eta_{b\to s} &= 1 \\ \eta_{s\to b} + \eta_{b\to b} &= 1. \end{aligned} \tag{62}$$

We can write the time partition coefficients for the body and surface waves as weighted averages of these time partition coefficients,

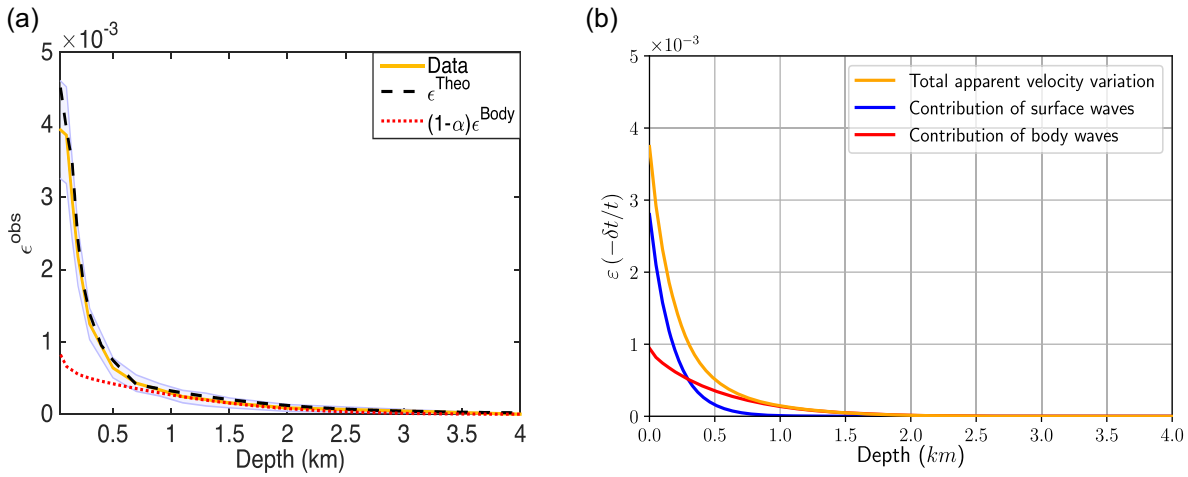

Figure 7. Apparent relative velocity variations with absorbing boundary conditions. Left: observed apparent velocity variations (orange), estimated contribution using only the body wave sensitivity (red) and modelled total apparent velocity variations (black)—modified from Obermann *et al.* (2016). Right: total apparent velocity variation (orange), contribution of body waves (red), and surface wave (blue) sensitivities estimated with the scalar sensitivity kernel.

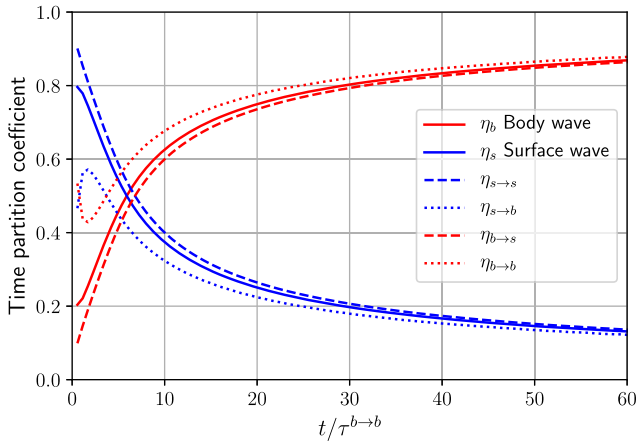

Figure 8. Evolution of the time partition coefficients for the surface (blue) and body (red) wave sensitivities, and as associated with each possible combination of mode of propagation and detection (dashed lines). The time is normalized by the body-to-body mean free time.

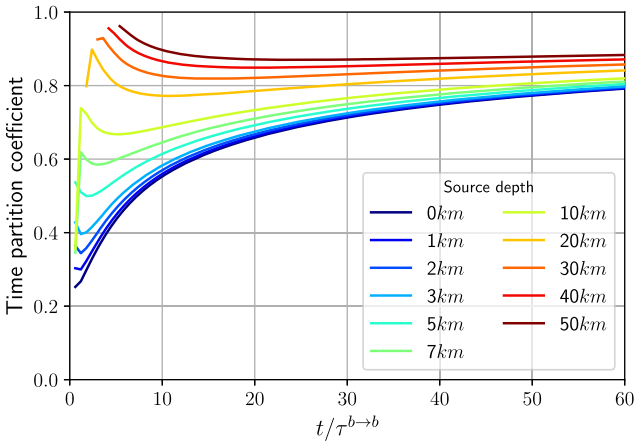

Figure 9. Body wave time partition coefficient for the different source depths. The parameters used for this series of simulations are shown in Table 1, with a surface penetration depth of $L_s = 10$ km and a body-to-body mean free path $l^{b\to b} = 10$ km.

following eq. (50)

$$\eta_s = \frac{E^s(t,r,z)}{E(t,r,z)}\eta_{s\to s} + \frac{E^b(t,r,z)}{E(t,r,z)}\eta_{s\to b}$$
$$\eta_b = \frac{E^s(t,r,z)}{E(t,r,z)}\eta_{b\to s} + \frac{E^b(t,r,z)}{E(t,r,z)}\eta_{b\to b}. \quad (63)$$

The evolution of the partition coefficients in time can be seen in Fig. 8. At very early lapse times, the time partition coefficient is strongly dominated by the surface waves, because the location of the source favours their excitation. This implies a predominance of the total surface wave sensitivity. The partition coefficients of the body and surface waves are equal (i.e. the crossing point) around 6 mean free time. This indicates the moment at which the body wave sensitivity starts to dominate the total sensitivity.

Fig. 8 also shows the dynamics of the coefficients classified by mode of propagation and detection. Just as before, the averages (i.e. solid lines) appear to be closer to the coefficients associated with the arrivals in the surface mode (dashed blue $\eta_{s\to s}$; red $\eta_{b\to s}$), especially at early lapse times. This is a consequence of the higher level of energy of the surface waves at the receiver that dominates the weighted average in eq. (63). Let us focus on the particles that arrive in the surface wave mode: in Fig. 8, the time partition $\eta_{b\to s}$ (red dashed line) is greater than $\eta_{s\to s}$ (blue dashed line) for long lapse times. This means that a surface wave particle arriving at the receiver has actually passed most of its traveltime propagating as a body particle. At this point, the difference of the time partition coefficient between the two modes of detection tends to disappear. This is the case, e.g., between $\eta_{b\to s}$ (red dashed line) and $\eta_{b\to b}$ (red dotted line), which converge.

8.4 Effects of source depth

The position of the source changes the overall participation of each type of wave in the sensitivity, as can be seen in Fig. 9. The time partition coefficient of the surface waves is omitted, as they are an exact counterpart of the body wave time partition coefficients. A source located far from the surface excites a lower amount of surface waves, which reduces the overall participation of surface waves in the sensitivity. This is seen at early times, when the body time partition coefficient increases with the source depth. For cases

where the source is located at 7 and 10 km in depth, the body time partition coefficient has an initial value between 0.3 and 0.4. This is the consequence of some early nonphysical arrivals produced by the low probability cases where the deep source excites the surface waves. This produces small quantities of energy that reach the receiver as soon as the source is activated, with times shorter than the traveltimes of the phonons. This is partially fixed using an energy threshold at the receiver, under which the sensitivity is not registered. Nonetheless, where these arrivals are still registered, it is easy to recognize the arrival of the body waves at the receiver, as they produce a maximum in the body time partition coefficient. It is from this point that the sensitivity takes on a physical meaning.

When the source is located beyond the reach of the surface waves (i.e. at depths over 20 km), the participation of the body waves is dominant at the beginning, and decreases as more paths are formed between the source and the receiver that pass through the propagation of the energy as surface waves. However, at long lapse times, the general systematic increase in the body time partition coefficient is common to all cases.

8.5 Symmetry relations

The mean free time is a natural scaling factor for time as it quantifies the degree of scattering. In a propagation medium without boundaries, two media with different mean free times at the same normalized time t/τ, will have similar distributions of energy and sensitivities if they are non-dimensionalized with mean free path. However, the introduction of the surface boundary in the half-space problem breaks this scaling. To understand why, it needs to be noted that the energy exchange between the two types of waves happens only in the zone close to the surface, within the reach of the surface waves. When a body particle is beyond this depth, the probability of turning back to a surface particle is close to zero. Therefore, a system with a small energy exchange zone will see a more rapid increase in the total body wave energy than a system with a larger exchange zone, on the assumption that they are equal in other aspects, such as the location of the source, and the mean free paths.

It is natural to introduce the ratio between the body-to-body mean free path and the penetration of the surface waves as a parameter of our model. We study the evolution of the time partition coefficients for different values of this ratio, fixing L_s at 10 km, and modifying $l^{b\to b}$ from 1 km to 100 km. The result is shown as the solid lines in Fig. 10 for the body waves. The curves representing the coefficients of the surface wave have been omitted for simplicity, as they contain the same information as the body wave coefficients. The general parameters that are used in this set of simulations are given in Table 2.

Fig. 10 shows that the total body sensitivity increases more quickly for the configurations with the higher mean free paths (represented in this case by the purple $l^{b\to b} = 100$ km and the red $l^{b\to b} = 50$ km lines), as in these cases the particles have greater chance to escape the exchange zone and the energy feedback into surface energy is lower. In the opposite cases (i.e. small mean free paths), the body wave particles tend to scatter often, and therefore remain for more time close to the surface, which increases the probability of turning into surface wave particles. Although the conditions of the source are equal between all the configurations (and therefore the initial proportions of energies between the two modes), the partition coefficient is higher for configurations with smaller mean free paths. This is because they have smaller receiver thickness (which is proportional to the mean free path, as can be seen in Table 2),

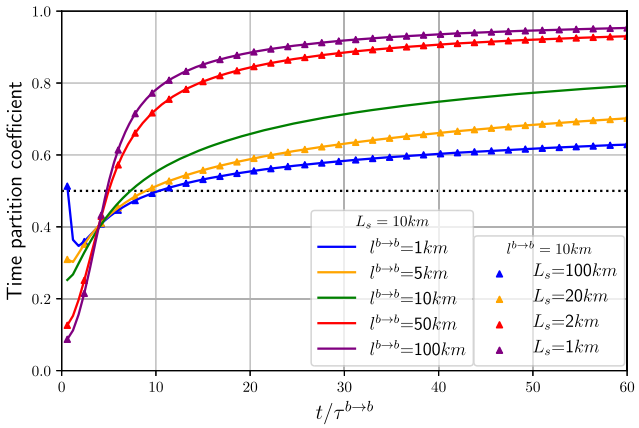

Figure 10. Body partition coefficients for different values of L_s and $l^{b\to b}$. Lines: time partition coefficients of body waves for a penetration depth of L_s = 10 km and different values of $l^{b\to b}$. Triangle scatter plots: time partition coefficients of body waves for a body-to-body mean free path of $l^{b\to b} = 10$ km and different values of L_s. The time is normalized by the body-to-body mean free time. The dotted black line indicates the level at which the body and surface time partition coefficients are equal (the crossing point).

Table 2. Parameters used in the Monte Carlo simulations for Section 8.5. The dimensions of the receiver zone are scaled with the mean free path.

Variable	Monte Carlo
Surface penetration depth L_s (km)	1, 2, 10, 20, 100
Body energy velocity c_E (km s^{-1})	3.9
Surface energy velocity c_R (km s^{-1})	4.1
Mean free path $l^{b\to b}$ (km)	1, 5, 10, 50, 100
Grid spacing g_r (m)	50
Receiver radius (km)	$4l^{b\to b}$
Receiver depth (m)	$l^{b\to b}/50$

which therefore covers a smaller part of the surface waves excited by the source (as the partition coefficients are calculated only with the particles that arrive at the receiver). This thickness does not affect the body waves, as these are excited in a single point over the surface.

Evaluation of how the relative proportions of $l^{b\to b}$ and L_s affect the evolution of the partition coefficient can also be achieved by fixing the mean free path and modifying the penetration depth of the surface waves. This is shown in Fig. 10 as the triangle scatter plots. It is evident that the evolution of the time partition coefficient has exactly the same behaviour as the scaled time. However, the interesting aspect of these results lies in the proportions: note, for example, that the values of $l^{b\to b}$ and L_s for the configuration represented by the blue line are one tenth of those for the configuration represented by the blue scatter plot. On the other hand, the values for the purple line are ten-fold their purple scatter plot counterparts. This means that the evolution of the sensitivity is completely determined by the adimensional ratio $l^{b\to b}/L_s$. In effect, all the configurations that share the same colour in Fig. 10 have completely different parameter values, but share the same $l^{b\to b}/L_s$ ratio.

The comparison of the sensitivity profiles with depth for the configurations in purple in Fig. 10 can be seen in Fig. 11. Their sensitivities are equal at different normalized depths, at the same normalized time. It is worth noting that in the two cases, the sensitivities extend through very different scales of length, and are captured at very different scales of time.

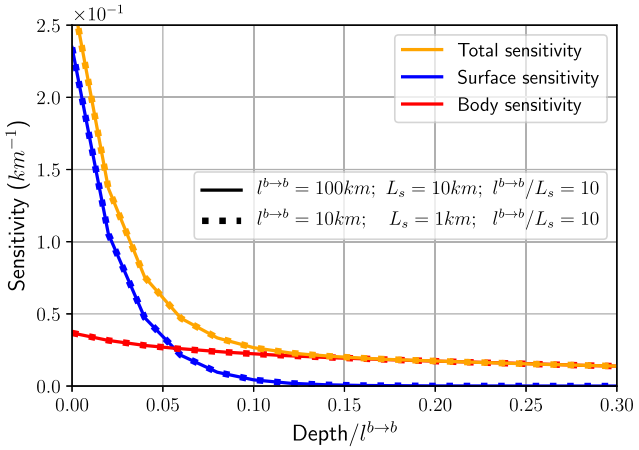

Figure 11. Total sensitivity (orange), body wave sensitivity (red), and surface wave sensitivity (blue) for configurations with $l^{b\to b} = 100$ km; $L_s = 10$ km (solid lines) and with $l^{b\to b} = 10$ km; $L_s = 1$ km (dashed lines), for a lapse time of $t/\tau^{bb} = 6$. The depth was scaled with their respective body-to-body mean free paths.

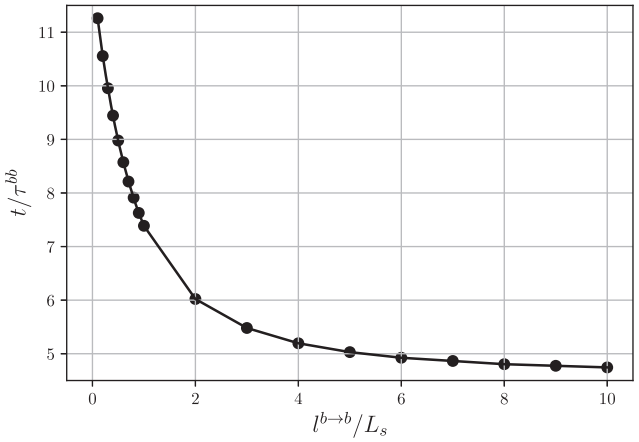

Figure 12. Normalized time at which the body and surface wave partition coefficients are equal for the different ratios of $l^{b\to b}/L_s$.

8.6 Crossing time

The crossing time of the time partition coefficient (i.e. the normalized time at which the surface and body wave time partition coefficients are both 0.5) marks the moment where the body wave sensitivity starts to be predominant over the surface wave sensitivity. We can see from Fig. 10 that this moment varies, depending on the value of $l^{b\to b}/L_s$. Fig. 12 shows the normalized time of the crossing point for systems for which the spatial scaling parameter $l^{b\to b}/L_s$ goes from 0.1 to 10 for a source located at the surface. When the mean free path is several times greater than the penetration depth ($l^{b\to b}/L_s \gg 1$), the coupling between surface and body waves is weak, and the crossing time decreases systematically. In the opposite case, where the mean free path is a lot smaller than the penetration depth ($l^{b\to b}/L_s \ll 1$), the sensitivity transition between surface and body waves is slower, as most of the body wave energy remains longer inside the energy exchange zone that is delimited by the surface wave, which produces increasingly greater crossing times.

9 CONCLUSIONS

We estimate the traveltime sensitivity kernels for a 3-D half-space based on the scalar case proposed by Margerin *et al.* (2019) that captures the natural coupling between body and surface waves. To achieve this, we approached the problem in several stages: first, we apply a variational approach to determine the response of the surface wave velocity to perturbations of the bulk velocity at different depths. After some simplifications, we reach an expression that relates these through the eigenfunction of the surface wave, which automatically sets the reach at which the sensitivity of the surface waves is relevant.

We reconstruct the sensitivity kernel formalism to include two possible modes of propagation, as surface and body waves, using a probabilistic description of the transit of phonons from the source to the receiver, which we extend towards different modes and depths. This also includes the modes of arrival at the receiver. The formalism presented here has the advantage that it can be easily extended to a full vectorial distribution of traveltime densities. It is shown that the traveltime sensitivity kernel can be expressed as the sum of two interdependent kernels associated with the sensitivity of surface and body waves.

The kernels are estimated through the measurement of time densities in Monte Carlo simulations. The initial set of parameters used are chosen to mimic as close as possible the work of Obermann *et al.* (2016), where estimations of the body and surface sensitivities were made with the help of full wavefield numerical simulations in the elastic case. Our model reproduces quantitatively well the traveltime changes observed in the numerical experiments of Obermann *et al.* (2016) which lets us foresee possible applications to real data.

The results show that the surface wave sensitivity is dominant at early times and limited to effective penetration equal to L_s. With increasing lapse times, the amplitude of the surface wave contribution to the sensitivity decreases, while its depth profile remains unchanged. This means that certain phase variations registered at the surface might be produced by different bulk velocity perturbations of different amplitudes that might be indistinguishable in an inversion problem with a single frequency measurement. This can be partially fixed by analysis of different penetration depths of the surface waves at several frequencies, as is implemented in inversions using surface waves. The body wave sensitivity, on the other hand, is less strong at the surface, but shows more interesting evolution, which includes progressive increase in its reach towards deeper zones of the medium. This confirms the critical role that the body wave sensitivity would have in the eventual application of the kernel to localize velocity perturbations in the medium.

The relative contribution of each mode of propagation to the total sensitivity can be estimated with the time partition coefficients. Their evolution shows the dominance of the surface wave sensitivity at early times, as the source and the receiver are both located in the same position in the surface. At later times, there is an increase and overall predominance of the body wave sensitivity, which is related to the continuous radiation of body wave particles into the bulk of the medium. We show how the initial conditions of the sensitivity are affected by increasing the source depth, which favours the body wave sensitivity.

Different scattering media with a single propagation mode have the same energy and sensitivity distributions when their spatial and temporal variables are non-dimensionalized with the mean free path and mean free time, respectively. However, introduction of the surface breaks this scaling, as media with equal scattering and source properties will show different energy distributions if the

size of the zone where the modes can scatter into each other is different. This energy exchange zone is delimited by the penetration of the surface waves, and is therefore independent of the scattering properties of the medium. The emergence of a characteristic scale length is observed in the evolution of the time partition coefficients. When the mean free path is considerably larger than the penetration of the surface waves, the body waves have more chance to propagate away from the exchange zone, which accelerates the overall increase in the body wave sensitivity. This can be interpreted as weak coupling between the two types of waves. In the opposite case, when the mean free paths are considerably smaller than the surface wave penetration depth, the eventual dominance of the body wave sensitivity is slower, as most of the body wave particles remain longer within the exchange zone and produce continuous energy feedback between the two modes of propagation.

However, we find a scaling principle between media that share the same scaling parameter $l^{b\to b}/L_s$, independent of the absolute values of $l^{b\to b}$ and L_s. We show that this invariance extends not only to the evolution of the time partition coefficients, but also to the sensitivities at depth, as long as the spatial and temporal quantities are non-dimensionalized with the mean free paths and times, respectively.

The moment at which the total body and surface wave sensitivities are equal to each other is defined as the crossing time, and this marks the moment at which the body waves start to dominate in the sensitivity. This happens in configurations that have the source close to the surface, so there is an initial predominance of the surface wave sensitivity. Analysis of the dependence of the crossing time with the ratio $l^{b\to b}/L_s$ shows that the strongest qualitative change occurs when this value is between 1 and 2. Increasing this ratio weakens the coupling between the modes, which produces a systematic decrease in the crossing time. A typical body-to-body mean free path of $l^{b\to b} = 100$ km with mean free times around $\tau^{b\to b} = 30$ s will result in dominance of the body wave sensitivity after 300 s for penetration depths up to $L_s = 10$ km. Therefore, to localize changes in the shallow crust, it is necessary to measure the $\delta t/t$ with very high precision in the part of the coda dominated by the surface wave sensitivity, or to have a favourably small mean free path (produced by highly heterogeneous media), such as in regions around volcanoes, where the mean free paths can be around 1 km (Yamamoto & Sato 2010).

Despite the natural limitations of the scalar description of wave propagation (e.g. the lack of polarization, the existence of a single mode of propagation for the body waves), our approach reproduces known features of the sensitivity with the advantage of requiring low computational resources. An extension of our approach to estimate the sensitivity kernels in a vectorial elastic medium is foreseeable in the future based on simulations of coupled body and Rayleigh waves (Xu *et al.* 2021).

ACKNOWLEDGMENTS

ERC F-image—This project has received funding from the European Research Council (ERC) under the European Union Horizon 2020 - Research and Innovation Framework Programme (grant agreement No. 742335). The authors want to thank Haruo Sato, Christoph Sens-Schönfelder and Ulrich Wegler for the careful review of this work and for their valuable input to improve it.

DATA AVAILABILITY

No third-party data were used in this study.

REFERENCES

Abubakirov, I.R. & Gusev, A.A., 1990. Estimation of scattering properties of lithosphere of Kamchatka based on Monte-Carlo simulation of record envelope of a near earthquake, *Phys. Earth planet. Inter.,* **64**(1), 52–67.

Aki, K., 1969. Analysis of the seismic coda of local earthquakes as scattered waves, *J. geophys. Res.,* **74**(2), 615–631.

Aki, K. & Chouet, B., 1975. Origin of coda waves: source, attenuation, and scattering effects, *J. geophys. Res.,* **80**(23), 3322–3342.

Aki, K. & Richards, P.G., 2002. *Quantitative Seismology,* 2nd edn, University Science Book.

Ben-Menahem, A. & Singh, S.J., 1981. *Seismic Waves and Sources,* Springer.

Brenguier, F., Campillo, M., Hadziioannou, C., Shapiro, N.M., Nadeau, R.M. & Larose, E., 2008. Postseismic relaxation along the San Andreas Fault at Parkfield from continuous seismological observations, *Science,* **321**(5895), 1478–1481.

Dahlen, F. & Tromp, J., 2021. *Theoretical Global Seismology,* Princeton University Press.

Gelfand, I. & Fomin, S., 1963. *Calculus of Variations,* Prentice Hall.

Gelfand, I.M. & Fomin, S.V., 2000. *Calculus of Variations,* Dover Publications, Inc.

Gusev, A.A. & Abubakirov, I.R., 1987. Monte-Carlo simulation of record envelope of a near earthquake, *Phys. Earth planet. Inter.,* **49**(1), 30–36.

Gut, A., 2013. *Probability: A Graduate Course,* Vol. 75, Springer Science and Business Media.

Hein, O., 2010. Green's functions and integral equations for the Laplace and Helmholtz operators in impedance half-spaces, *PhD thesis*, Ecole Polytechnique.

Hillers, G., Campillo, M. & Ma, K.-F., 2014. Seismic velocity variations at TCDP are controlled by MJO driven precipitation pattern and high fluid discharge properties, *Earth planet. Sci. Lett.,* **391,** 121–127.

Hoshiba, M., 1991. Simulation of multiple-scattered coda wave excitation based on the energy conservation law, *Phys. Earth planet. Inter.,* **67**(1–2), 123–136.

Hoshiba, M., 1997. Seismic coda wave envelope in depth-dependent *S* wave velocity structure, *Phys. Earth planet. Inter.,* **104**(1–3), 15–22.

Kanu, C. & Snieder, R., 2015. Time-lapse imaging of a localized weak change with multiply scattered waves using numerical-based sensitivity kernel, *J. geophys. Res.,* **120**(8), 5595–5605.

Lesage, P., Reyes-Dávila, G. & Arámbula-Mendoza, R., 2014. Large tectonic earthquakes induce sharp temporary decreases in seismic velocity in Volcán de Colima, Mexico, *J. geophys. Res.,* **119**(5), 4360–4376.

Lux, I. & Koblinger, L., 2018. *Monte Carlo Particle Transport Methods,* CRC Press.

Maeda, T., Sato, H. & Nishimura, T., 2008. Synthesis of coda wave envelopes in randomly inhomogeneous elastic media in a half-space: single scattering model including Rayleigh waves, *Geophys. J. Int.,* **172,** 130–154.

Margerin, L., Campillo, M. & Tiggelen, B., 1998. Radiative transfer and diffusion of waves in a layered medium: new insight into coda Q, *Geophys. J. Int.,* **134**(2), 596–612.

Margerin, L., Campillo, M. & Van Tiggelen, B., 2000. Monte Carlo simulation of multiple scattering of elastic waves, *J. geophys. Res.,* **105**(B4), 7873–7892.

Margerin, L., Planès, T., Mayor, J. & Calvet, M., 2016. Sensitivity kernels for coda-wave interferometry and scattering tomography: theory and numerical evaluation in two-dimensional anisotropically scattering media, *Geophys. J. Int.,* **204,** 650–666.

Margerin, L., Bajaras, A. & Campillo, M., 2019. A scalar radiative transfer model including the coupling between surface and body waves, *Geophys. J. Int.,* **219**(2), 1092–1108.

Meier, U., Shapiro, N.M. & Brenguier, F., 2010. Detecting seasonal variations in seismic velocities within Los Angeles basin from correlations of ambient seismic noise, *Geophys. J. Int.,* **181**(2), 985–996.

Miller, S. & Childers, D., 2012. *Probability and Random Processes: With Applications to Signal Processing and Communications,* Academic Press.

Obermann, A., Planès, T., Larose, E. & Campillo, M., 2013a. Imaging preeruptive and coeruptive structural and mechanical changes of a volcano with ambient seismic noise, *J. geophys. Res.,* **118**(12), 6285–6294.

Obermann, A., Planès, T., Larose, E., Sens-Schönfelder, C. & Campillo, M., 2013b. Depth sensitivity of seismic coda waves to velocity perturbations in an elastic heterogeneous medium, *Geophys. J. Int.,* **194,** 372–382.

Obermann, A., Froment, B., Campillo, M., Larose, E., Planès, T., Valette, B., Chen, J. & Liu, Q., 2014. Seismic noise correlations to image structural and mechanical changes associated with the M_w 7.9 2008 Wenchuan earthquake, *J. geophys. Res.,* **119**(4), 3155–3168.

Obermann, A., Planès, T., Hadziioannou, C. & Campillo, M., 2016. Lapse-time-dependent coda-wave depth sensitivity to local velocity perturbations in 3-D heterogeneous elastic media, *Geophys. J. Int.,* **207,** 59–66.

Obermann, A., Planès, T., Larose, E. & Campillo, M., 2019. 4-D Imaging of subsurface changes with coda waves: numerical studies of 3-D combined sensitivity kernels and applications to the M_w 7.9, 2008 Wenchuan earthquake, *Pure appl. Geophys.,* **176**(3), 1243–1254.

Pacheco, C. & Snieder, R., 2005. Time-lapse travel time change of multiply scattered acoustic waves, *J. acoust. Soc. Am.,* **118**(3), 1300–1310.

Pacheco, C. & Snieder, R., 2006. Time-lapse traveltime change of singly scattered acoustic waves, *Geophys. J. Int.,* **165**(2), 485–500.

Papoulis, A. & Pillai, S.U., 2002. *Probability, Random Variables, and Stochastic Processes,* Tata McGraw-Hill Education.

Planes, T., Larose, E., Rossetto, V. & Margerin, L., 2015. Imaging multiple local changes in heterogeneous media with diffuse waves, *J. acoust. Soc. Am.,* **137,** 660, doi:10.1121/1.4906824.

Poupinet, G., Ellsworth, W.L. & Frechet, J., 1984. Monitoring velocity variations in the crust using earthquake doublets: an application to the Calaveras Fault, California, *J. geophys. Res.,* **89**(B7), 5719–5731.

Przybilla, J., Korn, M. & Wegler, U., 2006. Radiative transfer of elastic waves versus finite difference simulations in two-dimensional random media, *J. geophys. Res.,* **111**(4), 1–13.

Ratdomopurbo, A. & Poupinet, G., 1995. Monitoring a temporal change of seismic velocity in a volcano: application to the 1992 eruption of Mt. Merapi (Indonesia), *Geophys. Res. Lett.,* **22**(7), 775–778.

Roepstorff, G., 2012. *Path Integral Approach to Quantum Physics: An Introduction,* Springer Science and Business Media.

Ross, S.M., 2014. *Introduction to Probability Models,* Academic Press.

Sanborn, C.J., Cormier, V.F. & Fitzpatrick, M., 2017. Combined effects of deterministic and statistical structure on high-frequency regional seismograms, *Geophys. J. Int.,* **210**(2), 1143–1159.

Sato, H., 1994. Multiple isotropic scattering model including *P–S* conversions for the seismogram envelope formation, *Geophys. J. Int.,* **117,** 487–494.

Schaff, D.P. & Beroza, G.C., 2004. Coseismic and postseismic velocity changes measured by repeating earthquakes, *J. geophys. Res.,* **109**(B10), doi:10.1029/2004JB003011.

Sens-Schönfelder, C. & Wegler, U., 2006. Passive image interferometry and seasonal variations of seismic velocities at Merapi Volcano, Indonesia, *Geophys. Res. Lett.,* **33**(21), doi:10.1029/2006GL027797.

Sens-Schönfelder, C., Margerin, L. & Campillo, M., 2009. Laterally heterogeneous scattering explains Lg blockage in the Pyrenees, *J. geophys. Res.,* **114,** doi:10.1029/2008JB006107.

Shearer, P.M. & Earle, P.S., 2004. The global short-period wavefield modelled with a Monte Carlo seismic phonon method, *Geophys. J. Int.,* **158**(3), 1103–1117.

Wang, Q.Y., Brenguier, F., Campillo, M., Lecointre, A., Takeda, T. & Aoki, Y., 2017. Seasonal crustal seismic velocity changes throughout Japan, *J. geophys. Res.,* **122**(10), 7987–8002.

Wegler, U. & Sens-Schönfelder, C., 2007. Fault zone monitoring with passive image interferometry, *Geophys. J. Int.,* **168**(3), 1029–1033.

Welch, A.J., Van Gemert, M.J.C. &Others, 2011. *Optical-Thermal Response of Laser-Irradiated Tissue,* Vol. 2, Springer.

Xu, Z., Margerin, L. & Mikesell, T.D., 2021. Monte Carlo simulations of coupled body- and Rayleigh-wave multiple scattering in elastic media, *Geophys. J. Int.,* **228**(2), 1213–1236.

Yamamoto, M. & Sato, H., 2010. Multiple scattering and mode conversion revealed by an active seismic experiment at Asama Volcano, Japan, *J. geophys. Res.,* **115**(B7), doi:10.1029/2009JB007109.

Zeng, Y., 2006. Scattered surface wave energy in the seismic coda, *Pure appl. Geophys.,* **163,** 533–548.

Zhang, T., Sens-Schönfelder, C. & Margerin, L., 2021. Sensitivity kernels for static and dynamic tomography of scattering and absorbing media with elastic waves: a probabilistic approach, *Geophys. J. Int.,* **225**(3), 1824–1853.

APPENDIX A: GROUP VELOCITY WITH FREQUENCY-DEPENDENT α

The frequency dependence of the parameter α introduced to trace a parallel with the elastic case has a collateral effect over the group velocity of the surface waves. We recalculate this velocity with the variational approach that was previously introduced. First, we estimate a perturbation of the eigenfunction both in $k_\parallel$ and in ω, $h + \delta h = h(k_\parallel + \delta k_\parallel, \omega + \delta\omega)$ in the energy integrals in eq. (27), to obtain

$$(\omega + \delta\omega)^2 (I_1 + \delta I_1) = (k_\parallel + \delta k_\parallel)^2 (I_2 + \delta I_2) + (I_3 + \delta I_3) - (I_s + \delta I_s'), \tag{A1}$$

where $\delta I_s'$ can be calculated from the definition of I_s' eq. (25), while bearing in mind that α is a frequency-dependent quantity

$$\delta I_s' = \frac{1}{2}\int_0^\infty \alpha T 2h\delta h\delta(z)dz + \frac{1}{2}\int_0^\infty \delta\alpha T h^2\delta(z)dz = \delta I_s + \frac{\delta\alpha}{\alpha} I_s. \tag{A2}$$

Subtracting eqs (27) and (26) from this expression, we find that

$$2\omega\delta\omega I_1 = 2k_\parallel\delta k_\parallel I_2 - \frac{\delta\alpha}{\alpha} I_s. \tag{A3}$$

and therefore the group velocity is

$$U = \frac{\delta\omega}{\delta k_\parallel} = \frac{k_\parallel}{\omega}\frac{I_2}{I_1} - \frac{\delta\alpha}{\delta k_\parallel}\frac{1}{2\alpha\omega}\frac{I_s}{I_1}. \tag{A4}$$

We start here to evaluate some of these integrals. I_2/I_1 can be calculated from their definitions

$$\frac{I_2}{I_1} = \frac{T\int_0^\infty h\delta h\mathrm{d}z}{\rho\int_0^\infty h\delta h\mathrm{d}z} = c^2. \tag{A5}$$

On the other hand, from eq. (7), it is clear that making α frequency dependent fixes c_R to a constant value. From this eq. (7), α is equal to

$$\alpha = \frac{\omega}{c}\sqrt{\left(\frac{c}{c_R}\right)^2 - 1}. \tag{A6}$$

Therefore,

$$\frac{\delta\alpha}{\delta k_\parallel} = c_R\frac{\delta\alpha}{\delta\omega} = \frac{c_R}{c}\sqrt{\left(\frac{c}{c_R}\right)^2 - 1} = \frac{c_R\alpha}{\omega}. \tag{A7}$$

Finally, to evaluate I_s and I_1, we make direct use of the eigenfunction $h = e^{-\alpha z}$:

$$I_1 = \frac{1}{2}\int_0^\infty \rho h^2 dz = \frac{1}{2}\rho\left(-\frac{1}{2\alpha}e^{-2\alpha z}\right)\Big|_0^\infty = \frac{\rho}{4\alpha}, \tag{A8}$$

$$I_s = \frac{1}{2}\int_0^\infty \alpha T h^2 \delta(z) dz = \frac{1}{2}\alpha T. \quad \text{(A9)}$$

Putting all of these together, we obtain

$$U = \frac{\delta\omega}{\delta k_\parallel} = \frac{c^2}{c_R} - c_R \frac{\alpha^2}{\omega^2} c^2 = \frac{c^2}{c_R} - c_R\left(\frac{c^2}{c_R^2} - 1\right) = c_R, \quad \text{(A10)}$$

which conveniently fixes the group velocity of surface waves with lower values than the velocity of body waves.

APPENDIX B: STATIONARITY OF THE LAGRANGIAN

Following Aki & Richards (2002, p.283), we find the perturbation of the eq. (24):

$$\begin{aligned}
&\omega^2\delta I_1 - k_\parallel^2 \delta I_2 - \delta I_3 + \delta I_s \\
&\quad = \omega^2 \int_0^\infty \rho h \delta h \mathrm{d}z - k_\parallel^2 \int_0^\infty T h \delta h \mathrm{d}z \\
&\qquad - \int_0^\infty T \frac{\mathrm{d}h}{\mathrm{d}z}\frac{\mathrm{d}\delta h}{\mathrm{d}z}\mathrm{d}z + \int_0^\infty \alpha T h \delta h \delta(z) \\
&\quad = \int_0^\infty \left\{\omega^2\rho h - k_\parallel^2 T h + \frac{\mathrm{d}}{\mathrm{d}z}\left(T\frac{\mathrm{d}h}{\mathrm{d}z}\right)\right\}\delta h \mathrm{d}z \\
&\qquad - T\frac{\mathrm{d}h}{\mathrm{d}z}\delta h\Big|_0^\infty + \alpha T h \delta h|_{z=0}\,. \quad \text{(B1)}
\end{aligned}$$

The terms inside the curly brackets correspond to applications of the wave eq. (1) for the surface eigenfunction, and are therefore equal to zero. The two remaining terms on the right-hand side of eq. (B1) are also equal to zero, noting that $\delta h = 0$ at $z = \infty$, and using the boundary condition $\mathrm{d}h/\mathrm{d}z|_{z=0} = -\alpha h|_{z=0}$.

Therefore, the integrated Lagrangian is stationary for a perturbation of the surface eigenfunction

$$\omega^2\delta I_1 - k_\parallel^2 \delta I_2 - \delta I_3 + \delta I_s = 0. \quad \text{(B2)}$$

APPENDIX C: INTEGRATION OF THE LAGRANGIAN FOR THE SURFACE WAVES

We apply eq. (1) over the surface wave solution in eq. (6), and multiply by $-h/2$, and integrate this over depth:

$$\begin{aligned}
0 &= \frac{1}{2}\int_0^\infty \rho\omega^2 h^2 \mathrm{d}z - \frac{1}{2}\int_0^\infty T k_\parallel^2 h^2 \mathrm{d}z + \frac{1}{2}\int_0^\infty T h \frac{\mathrm{d}^2 h}{\mathrm{d}z^2}\mathrm{d}z \\
&= \frac{1}{2}\int_0^\infty \rho\omega^2 h^2 \mathrm{d}z - \frac{1}{2}\int_0^\infty T k_\parallel^2 h^2 \mathrm{d}z - \frac{1}{2}\int_0^\infty T\left(\frac{\mathrm{d}h}{\mathrm{d}z}\right)^2 \mathrm{d}z \\
&\quad + \frac{1}{2} T h \frac{\mathrm{d}h}{\mathrm{d}z}\Big|_0^\infty. \quad \text{(C1)}
\end{aligned}$$

The first three terms are I_1, I_2 and I_3. Using the boundary conditions we can write the last term as follows :

$$-\frac{1}{2} T h \frac{\mathrm{d}h}{\mathrm{d}z}\Big|_0 = -\frac{1}{2} T h(-\alpha h)|_0 = \frac{1}{2}\int_0^\infty \alpha T h^2 \delta(z)\mathrm{d}z = I_s \quad \text{(C2)}$$

and therefore

$$\omega^2 I_1 = k_\parallel^2 I_2 + I_3 - I_s. \quad \text{(C3)}$$